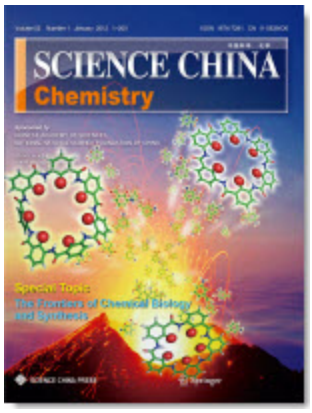

The role of oxygen vacancies in metal oxides for rechargeable ion batteries

Journal:	*SCIENCE CHINA Chemistry*
Manuscript ID	SCC-2021-0677.R1
Manuscript Type:	Review
Date Submitted by the Author:	07-Aug-2021
Complete List of Authors:	Wei, Runzhe; University College London, Chemistry Lu, Yi; University College London, Chemistry Xu, Yang; University College London, Chemistry
Keywords:	oxygen vacancies, defect chemistry, metal oxide, rechargeable ion batteries, ion diffusion, intercalation reaction, conversion reaction
Speciality:	Inorganic Chemistry

SCIENCE CHINA
Chemistry

• REVIEWS •

January 2016 Vol.59 No.1: 1–2

doi:

The role of oxygen vacancies in metal oxides for rechargeable ion batteries

Runzhe Wei,[1] Yi Lu,[1] and Yang Xu[1,*]

[1]*Department of Chemistry, University College London, 20 Gordon Street, London, UK WC1H 0AJ*

Received January 1, 2016; accepted February 2, 2016; published online March 3, 2016

Rechargeable ion batteries are one of the most reliable energy storage technologies for the applications ranging from small portable devices and electric vehicles to renewable energy integration and large-scale stationary energy storage. In the roadmap of developing and understanding new electrode materials for rechargeable ion batteries, oxygen vacancies, known as defects in metal oxides, have shown a high impact on the final electrochemical performance of the oxides. The present review aims to summarise the synthesis methods and characterisation techniques of oxygen vacancies as well as some of the most recent and exciting progress made to understand the role of oxygen vacancies in the electrochemical performance of Li-, Na-, K- and Zn-ion batteries. This review discusses not only the role of oxygen vacancies directly in electrode materials and indirectly in the coating layers on electrode materials but also the synergistic role of oxygen vacancies interplaying with other contributors such as carbonaceous materials, doping, amorphisation, structural transformation, nanostructuring and functional coating. Finally, perspectives are given to stimulate new ideas and open questions to facilitate the further development of oxygen deficient electrode materials in energy research landscape.

Keywords: oxygen vacancies, defect chemistry, metal oxide, rechargeable ion batteries, ion diffusion, intercalation reaction, conversion reaction

1 Introduction

Due to the severe environmental issues associated with the large amount of carbon dioxide emission caused by fossil fuels, there is a strong demand for sustainable energy sources and alternative energy storage [1-3]. Rechargeable ion batteries can reversely convert electric energy to chemical energy and are regarded as a promising energy storage technology [1,4]. The last three decades have seen the huge commercial success of lithium-ion batteries (LIBs). They not only have dominated the market of portable electronic devices but also are being highly pursued to fast pace the transition to electric vehicles, which plays a significant role in reducing the use of fossil fuels and the emission of carbon dioxide [5]. However, the rising cost and availability of

*Corresponding author (email: y.xu.1@ucl.ac.uk)

global lithium resources have raised concerns about the heavy reliance on LIBs and their massive production. In addition, the fact that stationary energy storage is indispensable for the deployment of renewable energies such wind and solar energy, and low-cost upon scaling up energy storage technologies is one of the basic requirements, for which the performance advantage of LIBs is outweighed by their rising cost.

In line with the effort to developing alternative rechargeable batteries with a low cost, and a few promising candidates have come to the spotlight in recent years, including sodium- [6-8], potassium- [9-11] and zinc-ion batteries [12-14] (SIBs, PIBs and ZIBs). SIBs and PIBs have a strong cost competitiveness against LIBs, because the Earth's abundance of Na and K is at least three magnitude higher than that of Li [6]. Furthermore, Al is much cheaper than Cu and could be used as the anode current collector, because Na and K do not form alloys with Al [15-16]. The commercial promise of SIBs and PIBs is engraved in the similar working mechanism between SIBs/PIBs and LIBs as well as the existing LIB industrial infrastructure that could be directly used for SIBs and PIBs. A recent theoretical study has shown that with respect to the weight of various components (anode, cathode, separator, and current collector) in a 18,650 battery cell, the energy density of a SIB (assuming $NaC_6/2Na_{0.5}CoO_2$, 231 Wh kg^{-1}) is only 20% lower than that of a LIB (assuming $LiC_6/2Li_{0.5}CoO_2$, 279 Wh kg^{-1}), and SIBs have no considerable advantage over PIBs (assuming $KC_6/2K_{0.5}CoO_2$, 218 Wh kg^{-1}) despite of the heavier weight of K compared to Na [17]. The cost competitiveness of ZIBs lies in the use of metallic Zn anode and aqueous electrolytes, which at the same time enables better safety and higher ionic conductivity (10^{-3} vs. 10^{-6} S cm^{-1}) compared LIBs with non-aqueous electrolytes. More importantly, the use of divalent Zn^{2+} as charge carrier and the feasibility of rapid Zn plating/striping allow multiple electron transfer during electrochemical reactions, offering the opportunity to simultaneously achieve high energy and power density (Fig. 1b).

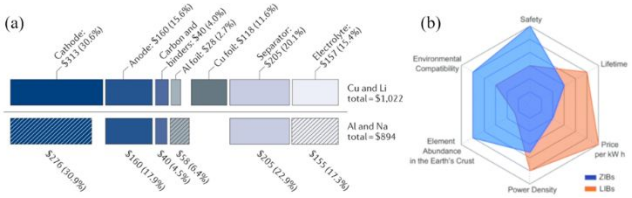

Figure 1. (a) Cost comparison of model SIBs and LIBs. Reproduce with permission [15]. Copyright 2018, Springer Nature. (b) Comparison of ZIBs and LIBs in various aspects. Reproduce with permission [12]. Copyright 2020, Royal Society of Chemistry.

Besides cost-competitiveness and promising electrochemical performance, the popularity of LIBs, SIBs, PIBs and ZIBs benefits from the utilisation metal oxides as electrode materials because of their low cost, diversity of synthetic methods and rich electrochemical processes [4]. However, intrinsically low electronic conductivity is one of the most common reasons to cause sluggish reaction kinetics of metal oxide electrodes and thus restrict the performance and wide application of metal oxides [4,18] One approach to overcome this problem is to fabricate composite materials that contain metal oxides and conductive carbonaceous materials [19-21]. The incorporation of carbonaceous materials enhances the electronic conductivity of the composites, leading to the better electrochemical properties of metal oxides as active materials. However, problems come along as carbonaceous materials lower the volumetric capacity of the entire electrode matrix and reduce the utilisation of active materials. Other issues including agglomeration of carbonaceous materials, cracking of metal oxides and poor interfacial interaction cannot be ignored [22-23]. Nanostructuring is another widely used approach to overcome the low electronic conductivity and sluggish reaction kinetics of metal oxides. This approach can enlarge the active surface area of metal oxides and shorten charge transfer distance, which facilitates ion and electron diffusion and improves reaction kinetics [18,24]. Although the two approaches have been proven beneficial, the intrinsic properties of metal oxide electrode materials remain largely unchanged, which calls for a facile but effective approach to regulate the intrinsic properties of

metal oxides and enhance their electrochemical performance. Oxygen vacancy (OV) is one of the most common defects in metal oxides due to a small formation energy and can have a profound impact on the capability of electrode materials. Utilising OVs has been investigated as a facile and effective strategy to regulate the intrinsic properties of metal oxide electrodes. Defect chemistry of OVs has been studied via theoretical methods [25-28]. OVs lead to the formation of cations with a lower oxidation state and thus lower electronegativity, which alters the electron chemical potential of the cations. In some metal oxides, OV state is formed within bandgap and acts as a donor state. Both effects result in the decrease of work function that is affected by electron affinity and bandgap. Since electron affinity is closer to be a material constant, the decrease of work function leads to a narrower bandgap [26,28]. Therefore, OVs can act as donors to improve the electronic conductivity of metal oxides. In addition, OVs as defects can also act as active sites for redox reactions during charge/discharge processes and accelerate ion insertion/extraction [4]. With the guidance of theoretical studies, OVs have been experimentally induced into a wide range of metal oxide electrode materials to tune their intrinsic properties and improve their electrochemical performance. These metal oxide electrodes range from diverse anode materials, such as TiO_2 [29], SnO_2 [30], MoO_3 [31], to various cathode materials with spinel and layered structures [25].

Given the success of metal oxides with OVs, this article aims to provide a comprehensive overview of recent progress of developing oxygen-deficient metal oxide electrodes for the battery applications including LIBs, SIBs, PIBs and ZIBs. Through summarising the synthesis methods of producing OVs, the measuring techniques of characterising OVs, and the electrochemical performance of oxygen-deficient metal oxide electrodes, we highlight the vital role of OVs in pushing forward battery technologies. In detail, we discuss not only the role of OVs directly presenting in electrode materials and indirectly presenting in the coating layers on electrode materials, but also the synergistic role of OVs interplaying with various contributors to determine the electrochemical mechanism and performance of metal oxides in a range of ion batteries. The contributors include carbonaceous materials, doping, amorphisation, structural transformation, nanostructuring and functional coating. We emphasise in this review article a role-oriented focus on OVs for charge storage (Fig. 2), in particular the synergistic role, which to the best of our knowledge is different from other review articles that are oriented by specific oxide materials with OVs [4,18,28]. Finally, we provide perspectives on studying oxygen-deficient metal oxide electrodes and hope to shed light on the potential future opportunities to investigate OVs for the battery application.

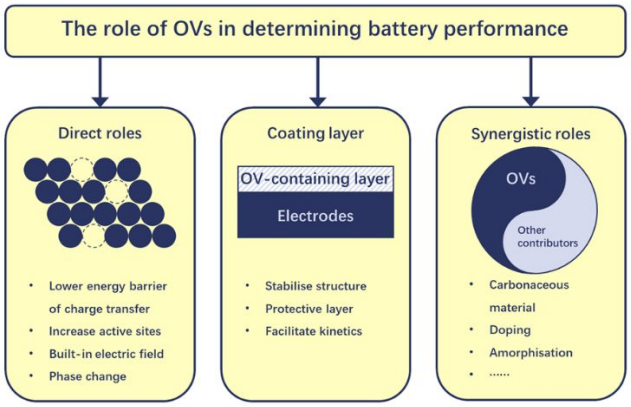

Figure 2. Schematic illustration of the focus and emphasis of this review article.

2 Synthesis of OVs in metal oxides

There has been a range of synthesis methods to create OVs in metal oxides and the methods can be classified into five categories as shown in Fig. 3: (i) heat treatment in oxygen deficient atmospheres, (ii) reducing agents, (iii) plasma treatment, (iv) carbonisation of organics, and (v) doping. As indicated by the names of the methods, there is a versatility of creating OVs in various reaction environments such as gas-, solution- and solid-phase, and there is also a diversity of creating OVs by using various reagents such as gases/compounds and inorganic/organic compounds. It is the versatility and diversity that makes OVs one of the most

studied defects in the battery research.

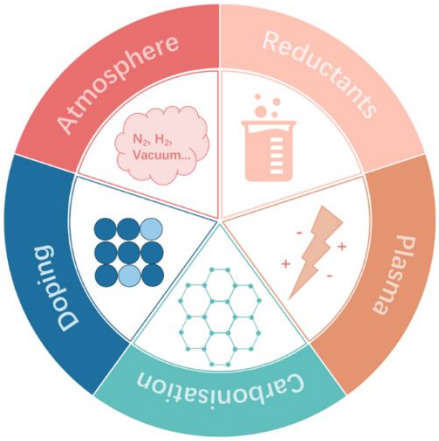

Figure 3. Schematic illustration of the synthesis methods to create OVs in metal oxides.

2.1 Heat treatment in oxygen deficient atmospheres

It can be traced back to 1991 when Nagoshi et al. proved that oxygen loss happened when a single crystal metal oxide was annealed in vacuum [32]. This process can be described by using defect chemistry, as shown below:

$$\frac{\beta}{2}O_2^{gas} + \alpha \cdot e^- + V_O \leftrightarrow O_\beta^{-\alpha}$$

where O_2^{gas} is an oxygen molecule in an ambient atmosphere, e^- is an electron which can reach the surface, V_O is unoccupied OVs, and $O_\beta^{-\alpha}$ is chemisorbed oxygen species. β=1 represents an atomic oxygen form, and β=2 represents a molecular oxygen form. α=1 is for single ionised oxygen species, and α=2 is for double ionised oxygen species [33,34]. With this inspiring and significant discovery, many researchers have been applying various annealing conditions to create OVs in metal oxides and using the oxides as electrodes for the rechargeable ion battery applications. Wu et al. annealed TiO_2 at 500˚C in a nearly vacuum condition (12 mTorr) for 2 h. The presence of OVs was evidenced by the peak at 531.6 eV in the O 1s X-ray photoelectron spectroscopy (XPS) spectrum of the obtained TiO_2, and resulted in enhanced SIB performance, especially better cycle stability compared to the OV-free TiO_2 [35]. A similar annealing condition was also used to obtain oxygen deficient TiP_2O_7 as an anode for LIBs [36].

In addition to vacuum condition, thermal annealing in an inert and/or reducing atmosphere can induce OVs in the metal oxides [30,37,38]. N_2 and Ar have been the most widely used inert atmospheres so far. Xu et al. annealed SnO_2 in N_2 atmosphere and air at 400˚C for 3 h, and they observed a strong signal at g = 2.003 in the electron paramagnetic resonance (EPR) spectrum of the N_2-annealed sample, suggesting the presence of OVs [39]. When used as an anode in SIBs, the oxygen deficient SnO_2 exhibited improved cycle stability and rate capability compared to its air-annealed counterpart. Liu et al. created OVs in Co_3O_4 by annealing it in Ar and adjusted the concentration of OVs by simply adjusting the temperature (150, 250 and 350˚C) [40]. The concentration of OVs analysed semi-quantitatively by deconvoluting the O 1s XPS peak did not increase monotonically with increasing the annealing temperature, where the highest concentration was achieved at 250˚C. Co_3O_4 with the maximum OVs concentration delivered the highest capacity and the best rate capability when tested in LIB half-cells, among all the Co_3O_4 samples [40]. Besides anode materials, there have also been reports on creating OVs in cathode materials by annealing them in an inert atmosphere. Luo et al. synthesised oxygen deficient $LiTi_2(PO_4)_3$, a NASICON-type LIB cathode, by annealing it in N_2 at 900˚C for 12 h [41]. After the thermal treatment, the colour of $LiTi_2(PO_4)_3$ changed from white to grey, which indicated the presence of mixed Ti^{4+}/Ti^{3+} caused by the generation of OVs. This resulted in the enhancement of electronic conductivity of $LiTi_2(PO_4)_3$ by nearly two orders of magnitude [41]. Xu et al. investigated oxygen deficient $LiMn_2O_4$ from the perspective of crystal chemistry. OVs were successfully generated in $LiMn_2O_4$ by annealing in Ar at 660˚C. With the increase of the annealing time and the concentration of OVs, Li_2MnO_3 phase was identified in addition to the dominant $LiMn_2O_4$ phase according to the

selected area electron diffraction (SAED) results [42]. Although the effects of OVs on the LIB performance was not studied explicitly, this type of phase change should be carefully treated during the battery application and will be discussed in section 4.1.4.

For reducing atmospheres, H_2/Ar and H_2/He mixtures have been widely used by employing the reducing power of H_2. Shin at el. annealed TiO_2, as a LIB anode, in both 5 vol% H_2/Ar and Ar atmosphere at 450˚C for 1 h. 5 vol% H_2/Ar annealed sample exhibited higher capacity and higher electronic conductivity than its Ar annealed counterpart [43]. More critically, by using a calculated defect model, the authors pointed out that the content of OVs can be adjusted by controlling the annealing time. Like annealing temperature, simply increasing annealing time did not lead to better electrochemical performance as 1 h-annealed sample delivered higher capacity and better rate capability than 7 h-annealed sample. Several examples have also been reported to introduce OVs into SnO_2 [44] and MnO anodes [45], by annealing them in 3 vol% and 5 vol% H_2/Ar atmosphere at 500˚C, respectively. In addition to anode materials, Abouimrane et al. successfully generated OVs in layered $Li_{1.12}Mn_{0.55}Ni_{0.145}Co_{0.1}O_2$ based on Li_2MnO_3-$LiMO_2$ (M=Mn, Ni, Co), by annealing the oxide in 3.5 vol% H_2/He atmosphere at 250˚C for 3 h [46]. XPS results showed that a small part of Ni^{3+} and Mn^{4+} was reduced to Ni^{2+} and Mn^{3+} due to the generation of OVs. Pure H_2 is another common reducing atmosphere and its utilisation can be traced back to 1959, when Cronzmeyer reduced rutile TiO_2 in H_2 to form OVs, making the treated TiO_2 semiconducting [47]. The colour of TiO_2 could change gradually from white to grey and even a darker colour with increasing annealing temperature and time, indicating the increasing amount of Ti^{3+} and OVs [48]. Compared to the results using H_2/Ar mixture [43], optimal annealing temperature and time were largely suppressed due the strong reducibility of H_2, which can be further confirmed by the results from Ma et al. [49]. Post-annealing in oxygen deficient atmospheres is a simple and facile method to generating OVs in metal oxide electrodes. Using an inert atmosphere also has a low risk level, but a relative high annealing temperature and/or long annealing time are necessary to obtain a desirable amount of OVs. In contrast, using a reducing atmosphere such as H_2 is more effective, due to the strong reducing power of H_2, but safety care needs to be taken into consideration. In addition, heat treatment in oxygen deficient atmospheres tends to be selective to metal oxides in which OVs have a relatively small reaction energy barrier [18].

2.2 Reducing agents

Being similar to a reducing atmosphere, a chemical that acts as a reducing agent can partially reduce metal ions in metal oxides during a reaction and thus create OVs in metal oxides [18]. There are two approaches to use reducing agents, depending on their presence in the reactions. The more common approach between the two is to directly mix a metal oxide or its precursor with a reducing agent before the reaction. It can occur in a solid-state reaction in the case of a solid reducing agent or a solution-phase reaction in the case of a liquid reducing agent. In addition, an inert atmosphere is required to avoid oxidisation in a solid-state reaction.

Tan et al. synthesised oxygen deficient Li_2MnO_3 by using $NaBH_4$ as a reducing agent, where pristine Li_2MnO_3 and $NaBH_4$ (1:2 in mass ratio) were annealed together in N_2 at 380˚C for 6 h. Reduced Li_2MnO_3 showed a significantly enhanced cathode capacity in LIBs compared to its OVs-free counterpart [50]. Due to the low valence of P in NaH_2PO_2, it has also been used as a reducing agent to generate OVs in metal oxides. Oxygen deficient $NiCo_2O_4$ was synthesised by annealing the material with NaH_2PO_2 in N_2 at 300˚C for 3 h [51]. Although OVs were successfully generated, P was detected on the surface of the sample by energy-dispersive X-ray spectroscopy (EDS). The same results were observed in oxygen deficient Co_3O_4, where NaH_2PO_2 was used as a

reducing agent [52]. The exact role of P remains unclear, however the authors claimed that the longer bond length and the lower electronegativity of the introduced P enhanced the surface reactivity of the electrode materials [51]. Carbon materials are another popular choice of reducing agents. Li et al. reduced pristine MoO_3 with carbon cloth in a sealed corundum crucible at 690˚C for 30 min [53]. The average valence state of Mo in MoO_{3-x} was 5 and the OV content was 0.5 per formula according to the deconvolution of the XPS spectra. The OV content was further adjusted by air annealing the oxygen deficient MoO_{3-x}, resulting in an average valence state of Mo to be 5.94 and even stoichiometric MoO_3 with prolonging the annealing temperature and time. It indicates that OV content can be reduced or even eliminated by annealing oxygen deficient metal oxides in air. Post-annealing in air is also essential to remove residual carbon in materials. Previous work [54] has shown that a small amount of residual graphene oxide was found in oxygen deficient $Li_4Ti_5O_{12}$ that was fabricated using graphene oxide as a reducing agent. So far, various inorganic reducing agents, including CaH_2 [55], LiH [55] and Mg [56] have been reported to create OVs in metal oxides. Besides solid chemicals, reducing solvents such as ethanol [57] and ethylene glycol [58] were used to directly create OVs in metal oxides. Chen et al. compared $Li_{1.2}Mn_{0.54}Ni_{0.13}Co_{0.13}O_2$ synthesised using ethanol and water as solvents and observed the presence of OVs in the sample synthesised in ethanol [59]. Solvothermal prepared sample showed enhanced cycle stability with a capacity retention of 80.4% after 100 cycles, which was about 40 % higher than the hydrothermal prepared counterpart as a cathode for LIBs. Furthermore, 46.1 mAh g^{-1} was remained at 3.75 A g^{-1} by the solvothermal prepared sample while the hydrothermal prepared sample only remained 5.4 mAh g^{-1}. It is worth noting that reducing agents, e.g., $NaBH_4$ [60], that are soluble in solvents can be used in a solution-phase reaction to create OVs in metal oxides, which often brings the benefit of a relatively low reaction temperature. Xiong et al. successfully generated OVs in MnO_2 at room temperature by stirring MnO_2 in a 0.1 M $NaBH_4$ solution, leading to enhanced capacity and rate capability as a cathode for aqueous ZIBs [60].

The second approach to use reducing agents is that they are in-situ formed during the reaction of synthesis, instead of being added before the reaction, hence creating a reducing environment to generate OVs in metal oxides. This approach is less commonly used than the first one, as reactions need to be carefully designed to realise the in-situ formation of reducing agents. A “sauna reaction” was used to fabricate OV-rich MoO_3 [61]. MoO_3, carbon cloth and a small amount of water were added in a hydrothermal reaction at 180˚C, during which carbon cloth reacted with H_2O vapor to release H_2 and CO, and OVs were formed in MoO_3 due to these reductive gases. Wang et al. reported an atomic substitution method to create OVs in TiO_2 [62]. By stirring TiS_2 in H_2O at room temperature for 72 h, S atoms were substituted by O atoms while reductive H2S was generated and subsequently reduced TiO_2.

Using reducing agents to create OVs in metal oxides could be beneficial if a high temperature is not required compared to thermal annealing in oxygen deficient atmospheres. However, some reducing agents can be highly reactive chemicals or combustive reductants, and safety issues need to be taken into consideration when designing reactions. In addition, residuals of reducing agents could exist after reactions, leading to contaminations or impurities in oxygen deficient metal oxides, which requires a careful post-reaction treatment to eliminate the residuals.

2.3 Plasma treatment

Plasma refers to a partially or fully ionised gas, and it is the fourth matter state. Compared to solid, liquid and gas states, plasma is in an electronically excited state and can provide a highly reactive environment for chemical reactions. It is a

facile method to create OVs in metal oxides using plasma due to its high energy [63,64]. Xu et al. first reported plasma treated Co_3O_4 for oxygen evolution reaction (OER) application [65]. Co_3O_4 was subjected to an Ar plasma treatment with a low power of 100 W for only 120 s. Besides the etching effect of plasma, OVs were created in Co_3O_4. Recently, plasma treatment has been used to generate OVs in metal oxides for rechargeable ion batteries. For example, $K_2Ti_6O_{13}$ anode was subjected to a 4 vol% H_2/Ar plasma treatment with a low power of 100 W for 2 h and without external heating [66]. For comparison, $K_2Ti_6O_{13}$ was also thermal treated in 5 vol% H_2/Ar atmosphere at 500˚C for 5 h. According to the XPS results, hydrogen plasma reduced more Ti^{4+} to Ti^{3+} and thus generated more OVs with a much lower temperature and a much shorter time compared to thermal treatment. The authors believed that plasma treatment is a more efficient way to induce OVs in metal oxides than heat treatment in oxygen deficient atmospheres. Another worth mentioning report is MoO_3 treated by H_2 plasma with a constant power but different time duration to achieve an optimal content of OVs [67]. N_2 plasma is another commonly used plasma treatment. Lan et al. successfully induced OVs into $Li_4Ti_5O_{12}$ by using N_2 plasma treatment [68]. However, the authors observed the existence of N in the XPS spectra, indicating a certain level of N-doping in the treated samples, because some O^{2-} in the structure is substituted by N^{3-} after the plasma treatment. Besides H_2, Ar and N_2 plasma, air plasma has also been reported [69,70]. Plasma treatment is a convenient method to create OVs owing to the high reactivity of plasma, a very short time of the treatment, and the elimination of high temperature. However, the cost of plasma treatment is relatively high compared to annealing in oxygen deficient atmospheres and using reducing agents. The morphology of samples could slightly change sometimes due to the etching effect of plasma [64].

2.4 Carbonisation of organics

Carbonisation of organic materials in an oxygen-deficient atmosphere has been used to prepare composites of oxygen deficient metal oxides and carbons. During the carbonisation, non-C-C bonds break with the sufficient activation energy gained from a high temperature, and the resulting carbon structure is protected from being oxidised by the oxygen-deficient atmosphere. It is because the absence of oxygen in the environment that the carbonisation of organic materials extracts the lattice oxygens from metal oxides and create OVs. The selection of organometallic compounds as reaction precursors is key to simultaneously obtain target metal oxides and the creation of OVs. Zhang et al. reported a one-step solid-state reaction by using LiOH and $VO(C_5H_7O_2)_2$ as precursors to synthesise Li_3VO_4 [71]. After being treated in an Ar atmosphere at 600˚C for 2 h, the organic moiety in $VO(C_5H_7O_2)_2$ decomposed and formed carbon, and at the same time OVs were created in Li_3VO_4, which was proven by the Raman and XPS results. Compared to Li_3VO_4, the oxygen deficient Li_3VO_4/C composite exhibited better electrochemical performance as an anode in LIBs due to fast Li^+ and electron transport. A similar solid-state reaction in an Ar stmosphere was reported to fabricate $K_2V_8O_{21}$/C composite with rich OVs in $K_2V_8O_{21}$ [72]. Carbon and OVs were produced by the carbonisation of the organic precursor $C_6H_7KO_7$. In addition, TiP_2O_{7-x}/C [73] and TiO_{2-x}/C [74] were also reported as examples for carbonising organic precursors hexachlorophosphazene and titanium(IV) bis(ammonium lactate)dihydroxide, respectively.

Instead of using organometallic compounds, another approach to create OVs by the carbonisation of organic materials is to separately add organic materials as carbon sources in the carbonisation reaction. Zhang et al. used glucose as a carbon source to fabricate K_xTiO_2/C composite [75]. Glucose was mixed with as-prepared $K_2Ti_6O_{13}$ and the mixture was further treated in a N_2 atmosphere at 800˚C for 6 h. During the carbonisation of glucose, $K_2Ti_6O_{13}$ was

coated by a carbon layer, and at the same time Ti was partially reduced to generate oxygen deficient K_xTiO_2. Wu et al. thermally treated TiO_2 with poly-4-vinylpyridine (P4VP) in an Ar/H_2 atmosphere at 600˚C for 3 h [76], where the carbonisation of P4VP resulted in a N-doped carbon layer on the surface of TiO_2 and OVs in TiO_2. Moreover, Sun et al. reported that OV content can be adjusted by changing the amount of organic materials [77]. OVs were generated in Li_2MnO_3 by using various amount of stearic acid (1:0.03, 1:0.04, 1:0.05 in mole ratio). The increasing amount of stearic acid led to an increasing OV content. However, excessive stearic acid caused the formation of a secondary phase of $LiMnO_2$ [77]. Therefore, an appropriate amount of organic materials is essential to balance between enhanced electrochemical performance of metal oxides and undesirable impurities. It is worth mentioning that electrospinning technique has been reported to fabricate one-dimensional (1D) oxygen deficient metal oxide/carbon composites [78]. For instance, a mixed suspension of Ti precursor and polyacrylonitrile (PAN) was spun by the electrospinning technique [79], and then the as-spun fibres were thermally treated in an inert atmosphere to carbonise PAN, which finally resulted in oxygen deficient TiO_2 anchored in N-doped carbon fibres.

Carbonisation of organic materials or organic moiety of precursors is a facile and mild approach to create OVs in metal oxides. The resulting carbon often attributes to the improved electrochemical performance of metal oxides by improving the electronic conductivity and/or maintaining the structural integrity of the oxides during repetitive ion insertion/extraction. However, this approach is in general lack of the control on the composition and structure of the final products, due to the little control on the carbonisation of organic materials, making it difficult to adjust the OV content in the final products.

2.5 Doping

Heterogeneous doping can create unbalanced charge ambience and/or lattice distortion in metal oxides and lead to the formation of OVs [18]. Heterogeneous doping can be either cationic or anionic. As an example of cationic doping, Xia et al. created OVs in $Na_2Ti_3O_7$ by doping a series of lanthanide (Ln) elements, including La, Ce, Nd, Sm, Gd, Er, and Yb [80,86]. The XPS results showed that a small quantity of Ti^{4+} was reduced to Ti^{3+}, due to the doping of Ln elements. The existence of low valence cations such as Ti^{3+} and Ln^{3+} caused unbalanced charge and further led to the generation of OVs in $Na_2Ti_3O_7$. Although all the doped $Na_2Ti_3O_7$ exhibited enhanced electronic conductivity and better electrochemical performance, it is notable that different doping elements showed different level of improvement, and Yb-doped $Na_2Ti_3O_7$ provided the best performance. The authors pointed out that the reason behind this phenomenon remained to be studied [80]. Another worth mentioning example is Mn/Ni co-doped CoO [81]. Due to the larger radii of Mn^{2+} and Ni^{2+} (67 and 69 pm, respectively) compared to that of Co^{2+} (65 pm), the interspace of O^{2-} was squeezed, which resulted in OVs. Furthermore, Li et al. found that more OVs were generated with an increasing amount of doped Mn^{2+} and Ni^{2} and the authors successfully adjusted the OV content by extending the reaction time due to the relatively slower reaction rate of Mn^{2+} and Ni^{2+} compared that of Co^{2+} [82]. As an example of anionic doping, He et al. synthesised oxygen deficient N-doped TiO_2 through a small part of O^{2-} being substituted by N^{3-} [83]. The extra electron offered by N^{3-} resulted in the reduction from Ti^{4+} to Ti^{3+} and the formation of OVs to compensate the charge [84]. Liu et al. doped S into Nb_2O_5 by directly heating the sample with S powders in an Ar atmosphere [85]. Lattice distortion was induced because the radius of S^{2-} is 30% larger than that of O^{2-}. As a result, Nb^{4+} and OVs were formed, which led to the improved electrochemical performance of S-doped Nb_2O_5 as a SIB anode. Since charge unbalance and lattice distortion are caused by dopants, the resulting OVs are less possible to

be oxidised compared to other synthesis methods of OVs [86]; hence, doped metal oxides with OVs are relatively stable. However, doping heterogeneous elements could induce impurities. The effect of dopants is positive, neutral, or even negative depending on many factors and can be varied from oxide to oxide.

3 Characterisation of OVs in metal oxides

3.1 X-ray photoelectron spectroscopy

XPS is a widely used characterisation technique to quantitatively investigate elemental composition and chemical and electronic status at the surface of materials. It is worth mentioning that OVs cannot be directly observed by XPS as an OV is not an electronic state but a vacant position in the lattice due to the absence of an oxygen ion; as a result, OVs are characterised by XPS in an indirect way. An O 1s XPS spectrum of metal oxide could consist three components. The low O 1s binding energy range from 527.7 to 530.5 eV corresponds to O^{2-} ions, representing the typical metal-oxygen bonds in a metal oxide [87]. The medium O 1s binding energy range from 531.1 to 532 eV has been described as a signal of OVs in many literatures. Formally, this energy range corresponds to the O^- species that bear a lower electron density than the regular O^{2-} ions. The existence of O^- species represents low coordinated oxygen ions with a higher covalence of a metal-oxygen bond. In other words, this signal can be regarded as a compensation of oxygen deficiency in a metal oxide [88,89]. The high O 1s binding energy range from 532 to 533 eV corresponds to the weakly absorbed species on the surface of metal oxides, such as H_2O and -CO_3 [88,90]. Fig. 4a shows the O 1s XPS spectrum of Fe_2O_3, where three components labelled as O_I, O_{II} and O_{III} were observed at 530.1, 531.3 and 532.6 eV, respectively. O_I represents the lattice oxygen in Fe_2O_3, while O_{II} is associated with the OVs in the oxide. O_{III} represents the surface absorbed group [89]. Moreover, the ratio of the oxygen species can be obtained by calculating the relative peak areas of the three components (Fig. 4b) [90,91]. High resolution XPS spectra of metal elements can be used to complement the characterisation of OVs. Fig. 4c shows the Mn 2p spectra of oxygen deficient $K_{0.8}Mn_8O_{16}$ [92]. Compared to α-MnO_2, the blue peaks of $K_{0.8}Mn_8O_{16}$ have lower binding energies that are representative for Mn^{3+}, and the increased peak intensity indicates that partial Mn^{4+} were reduced to Mn^{3+} due to the existence of OVs. Despite XPS cannot directly detect OVs, it is an effective way to reflect the presence of OVs in metal oxides and a relative OV content can be obtained by calculating peak areas. However, XPS is a surface sensitive characterisation technique, and it can only provide the signals from a subsurface of samples.

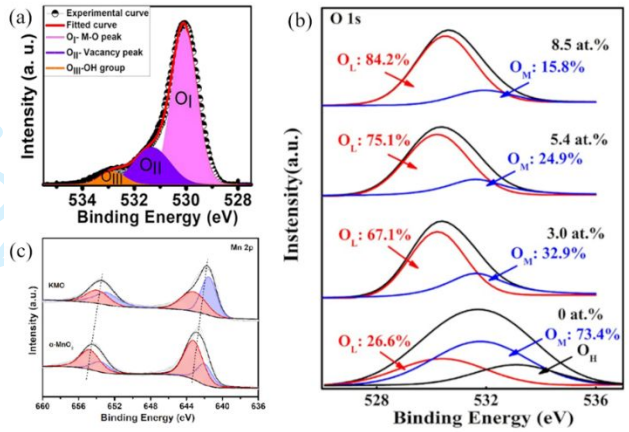

Figure 4. (a) O 1s XPS spectrum of α-Fe_2O_3. Reproduce with permission [89]. Copyright 2019, Wiley-VCH. (b) O 1s XPS spectrum of SnO_2 with different Si doping content from 0 to 8.5 at.%. Reproduce with permission [91]. Copyright 2016, Wiley-VCH. (c) Mn 2p XPS spectrum of $K_{0.8}Mn_8O_{16}$ and α-MnO_2. Reproduce with permission [92]. Copyright 2019, Wiley-VCH.

3.2 X-ray absorption fine spectroscopy

X-ray absorption fine spectroscopy (XAFS) is a powerful characterisation technique to study electronic states and atomic geometry in a local environment. XAFS includes two parts, X-ray absorption near-edge spectroscopy (XANES) and extended X-ray absorption fine-structure spectroscopy (EXAFS). XANES gives the information of the absorbing atom, including its valence state and electronic structure.

EXAFS studies the local atomic geometry of the absorbing atom, which gives information of bond length, coordination number and disorder degree [93]. Atomic and electronic structure change caused by OVs can be detected by XAFS, which in turn proves the presence of OVs. Zhang et al. used XANES to capture the chemical state change caused by OVs in the H_2 plasma-etched MoO_3 [67]. As shown in the Mo K-edge XANES spectra (Fig. 5a), the pre-edge peak at 20006 eV refers to the 1s to 4d electron transfer in the distorted MoO_6 octahedra, which is a typical feature of α-MoO_3 with Mo^{6+} valence state [94]. The peak slightly shifted to a higher energy with a decreased peak intensity as the etching time of α-MoO_3 increased, which indicates the increased oxygen loss during the etching process. The two peaks located between 20020 and 20040 eV (Fig. 5a) shifted to a lower energy with an increased peak intensity as the etching time increased, which indicates the increasing amount of Mo with a lowered valence state in the etched MoO_3 samples [67]. In addition to the chemical state change of metals detected by XANES, the structural distortion caused by OVs can be detected by EXAFS. Leedahl et al. used O K-edge EXAFS spectra to investigate the structural distortion of black TiO_2 that features bulk of OVs [95]. As shown in Figs. 5b and 5c, the coordinating information of the central O atom can be seen by the significant reduction in Ti-O distances. The nearest Ti-O bond length for anatase TiO_2 was 1.95 Å and it was reduced to 1.89 Å in black TiO_2. The next Ti-coordination site was reduced from 3.86 Å to 3.84 Å. The further Ti-coordination site at 4.26 Å was reduced to 4.17 Å. Due to the existence of OVs, the degeneracy of O-O distances and Ti-O distances in the pristine anatase was broken, e.g., the nearest 6 O-coordination sites between 2-3 Å splitting into various distances. The authors concluded that, in black TiO_2, Ti atoms tend to slightly shift away from OVs for a better bonding to the rest of the lattice, while O atoms tend to slightly move towards OVs to fill the vacant places [94]. Therefore, XANES has a strong ability to analyse the atomic and electronic structure change caused by OVs, and EXAFS can investigate the actual structural distortion caused by the existence of OVs at a very precise scale. It is worth noting that XAFS does not rely on the periodicity of crystal structures, as seen in the study of the electronic structure change and lattice distortion of OVs-containing amorphous MoO_3 [96]. However, the availability of XAFS heavily depends on the use of central or national facilities.

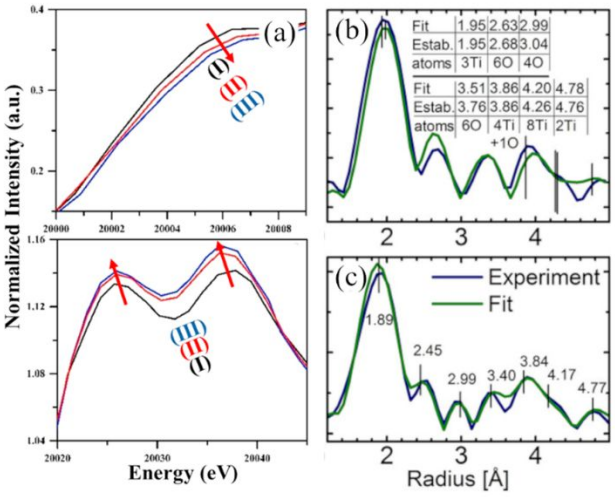

Figure 5. (a) The pre-edge peaks (upper) and the edge peaks (lower) of Mo K-edge XANES spectra (I: 0 minute etching; II: 10 minutes etching; III: 20 minute etching). Reproduce with permission [67]. Copyright 2018, Elsevier; Fourier transforms of EXAFS signals of (b) TiO_2 and (c) oxygen deficient TiO_2. Reproduce with permission [95]. Copyright 2019, Wiley-VCH.

3.3 Electron paramagnetic resonance

EPR can detect unpaired electrons in materials through the interaction between an applied external magnetic field and the unpaired electrons that generate resonance when the field is swept [97]. Two unpaired electrons are expected to be generated by each OV, and they could be trapped in the proximity to the oxygen site [98]; therefore, EPR is sensitive to the single electron trapped OVs. The typical EPR signal of OVs is often found at around g = 2.000-2.008 [99], where g is the Landé g-factor. Zheng et al. recorded the EPR spectra of TiO_2 that was thermal treated in a H_2 atmosphere at different temperatures [100]. Compared to pristine TiO_2, thermal treated TiO_2 at 500˚C (H-TiO_2-500) showed a strong EPR signal at g = 2.001 (Fig. 6a), indicating the presence of

OVs. With increasing the temperature of the thermal treatment, the intensity of the EPR signals increased (Fig. 6b), indicating the increased amount of OVs at higher temperatures [100]. Despite being used to characterise OVs in metal oxides, it is worth noting that previous studies have shown the limitation of EPR [101,102]. The studies pointed out that EPR can only detect single electron trapped OVs due to the principle of EPR, whereas OVs with no electron or two electrons do not show signals in an EPR spectrum, but OVs with two electrons can be detected indirectly in some cases. For example, in oxygen deficient TiO_2, the two electrons trapped by an OV were localised on two neighbouring Ti^{4+}, forming a pair of paramagnetic Ti^{3+} which has an EPR signal at g = 1.94-1.99 [100,103]. As shown in Figs. 6a and 6c, the EPR signal of Ti^{3+} can be regarded as the evidence of the presence of two electrons trapped OVs. This limitation of EPR is essential, because bulk OVs and surface OVs tend to trap different numbers of electrons [101], which needs to be taken into consideration when characterising OVs using EPR.

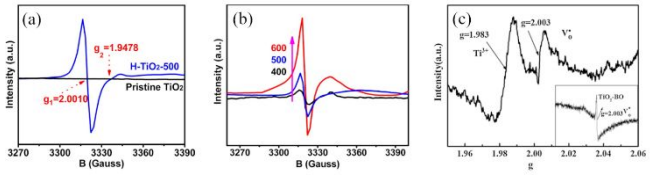

Figure 6. EPR spectra of (a) pristine TiO_2 and H-TiO_2-500; (b) TiO_2 treated at different temperature (400°C, 500°C and 600°C). Reproduce with permission [100]. Copyright 2015, American Chemical Society; (c) EPR spectra of TiO_2 with both bulk OVs and surface OVs. Reproduce with permission [102]. Copyright 2017, Elsevier.

3.4 Positron annihilation lifetime spectroscopy

Positron annihilation lifetime spectroscopy (PALS) is capable of not only detecting the presence of vacancies but also providing information of the size, type and relative concentration of the vacancies. Once positrons are emitted to a material, they can be annihilated through interacting with electrons and the annihilation releases γ-ray that in turn is detected [104]. The time between the emission of positrons and the detection of γ-ray is regarded as the lifetime (τ) of positrons, which is closely related to the size and type of vacancies and consists of three components, τ_1, τ_2 and τ_3 with the corresponding intensities I_1. I_2 and I_3. Free annihilation of positrons in vacancy-free crystals generates the shortest lifetime (τ_1). However, smaller vacancies (e.g., monovacancy) can reduce the surrounding electron density, leading to an increased τ_1. τ_2 is longer, as it is attributed to positrons captured by defects with a larger area (e.g., vacancy clusters), which causes an even lower electron density and hence decreases the annihilation rate and extends the lifetime. Furthermore, the I_1/I_2 ratio can be used to estimate the relative concentration of small sized vacancies to large sized vacancies. τ_3 is the largest among the three and it is ascribed to an even larger cluster (nanoscale) of vacancies [100,104-106]. Jiang et al. compared the PALS spectra and the resolved τ of pristine TiO_2 (P25) and TiO_2 treated in H_2 (H-P25) (Fig. 7) [104]. H-P25 exhibited a remarkably higher τ_1 (188.1 ps) than P25 (140.5 ps), and the I_1 of H-P25 was also increased from 11.22% to 14.30%. This indicates that the H_2 treatment has produced a large number of small sized OVs. H-P25 showed a slightly increase of τ_2 from 376.9 to 378.7ps, indicating that the number of larger sized oxygen vacancy clusters almost remained unchanged after the treatment. τ_3 was not detected in P25 but was detected in H-P25 (19.3 ns), which means some voids of OVs in nanoscale were created though I_3 remained very low (0.25%) [104]. It is worth noting that, in the case of TiO_2 [106] and ZnO [107], small sized OVs tend to exist in the bulk of the materials, and larger sized OV clusters mainly exist in the near surface area of the materials. Therefore, τ_1 and τ_2 can be regarded as a sign of bulk OVs and surface OVs, respectively. PALS is a sensitive and powerful characterisation method to study different types of OVs, and it would be encouraging to see an increase in utilising PALS for the battery research.

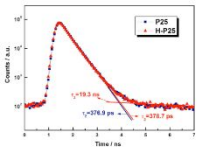

sample		τ_1 (ps)	τ_2 (ps)	τ_3 (ns)	I_1 (%)	I_2 (%)	I_3 (%)
P25	value	140.5	376.9	NA	11.22	88.78	NA
	deviation	14.1	2.1	NA	1.08	1.08	NA
H-P25	value	188.1	378.7	19.3	14.30	85.45	0.25
	deviation	19.9	3.8	10.7	2.74	2.75	0.07

Figure 7. PALS spectra of P25 and H-P25, and resolved τ with corresponding

intensities. Reproduce with permission [104]. Copyright 2012, American Chemical Society.

3.5 Transmission electron microscopy

In contrast to the spectroscopies mentioned above, transmission electron microscopy (TEM) is a characterisation technique that gives direct visual proof of OVs in metal oxides and more importantly, an atomic resolution is required to deliver such kind of visual proof. Li et al. used annular bright field TEM (ABF-TEM) to image the OVs in Mn/Ni co-doped CoO along the [110] direction [82]. As shown in Figs. 8a and 8b, the large black dots corresponded to Co^{2+}, Mn^{2+} and Ni^{2+}, and the small black dots corresponded to O^{2-} due to the larger mass of the metal ions. Figs. 8c-e show the signal intensities of the marked three location pathways (in yellow rectangles in Figs. 8a and 8b). The peaks with a significantly lower intensity (in red dash rectangles) indicated the existence of OVs at the corresponding spots (circled in red) in Fig. 8b. In addition to ABF-TEM, other advanced TEM technologies, such as diffraction mode [108], annular dark field (ADF) [109], and high-angle annular dark field (HAADF) [110], are also able to direct images of OVs or capture the lattice distortion caused by OVs. As a visual characterisation technique, TEM can be used to investigate oxygen deficient metal oxides from a different view from spectroscopic techniques, but as afore-mentioned, ideally an atomic resolution with advanced characterisation modes is essential; hence increasing the availability of this technique is key to amplify its benefit in investigating OVs.

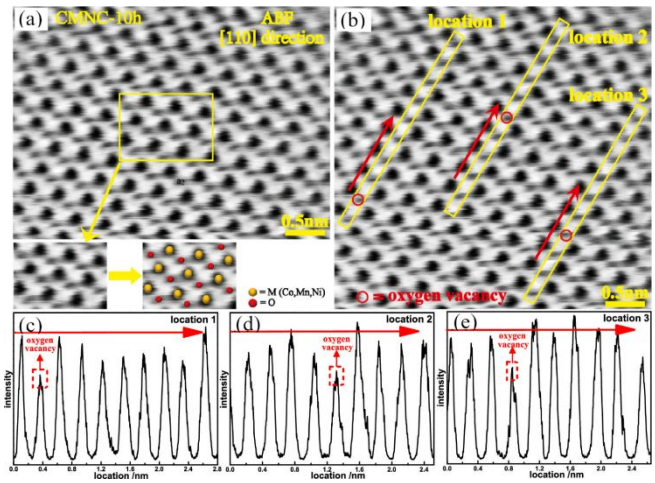

Figure 8. (a)(b) ABF image of Mn/Ni co-doped CoO; (c-e) signal intensities of O^{2-} ion columns in corresponding regions marked in (b). Reproduce with permission [82]. Copyright 2019, American Chemical Society.

4 The role of OVs in determining the electrochemical performance of metal oxide electrodes

4.1 The direct role of OVs

OVs can be a major contributing factor to enhance the electrochemical performance of metal oxide electrodes. There has been a large number of literature reporting the direct role of OVs on the intrinsic properties of metal oxides, and the role can be summarised into four aspects: (i) enhancing electronic conductivity and reducing ion diffusion energy barrier, (ii) increasing active sites to store ions, (iii) inducing built-in electric field, and (iv) causing phase change.

4.1.1 Enhancing electronic conductivity and reducing ion diffusion energy barrier

Introducing OVs can cause the change in the electronic structures of metal oxides, which results in the enhancement of electronic conductivity [111]. Chen et al. demonstrated this kind of enhancement by comparing the density of state (DOS) and partial DOS (PDOS) patterns between oxygen deficient TiO_2 (anatase-OV) and pristine TiO_2 (anatase), as well as between Na inserted anatase-OV and Na inserted anatase, via density functional theory DFT calculations [112].

The Fermi level of anatase-OV (Fig. 9a) shifted to the conduction band, meaning electrons were the main charge carriers in this structure. Moreover, Ti 3d state was delocalised upon the introduction of OVs, which increased the width of conduction band. Therefore, the band gap of TiO_2 was narrowed, leading to the improvement in electronic conductivity. This was in an agreement with the experimental results. The electronic conductivity dramatically increased from 2.1×10^{-8} S cm^{-1} for pristine TiO_2 to 4.3×10^{-4} S cm^{-1} for oxygen deficient TiO_2. After Na^+ insertion (Fig. 9b), the conduction and valance bands both moved negatively, while a smaller extent of movement was observed for Na inserted anatase-OV compared to Na inserted anatase. The electron orbits of Ti, O and Na of Na inserted anatase-OV overlapped in more parts compared to those of Na inserted anatase, indicating a higher activity towards Na^+ for the former. It was reflected by the lower sodiation energy of anatase-OV (4.75 eV) than that of anatase (5.63 eV), suggesting the energetically favourable for Na^+ insertion in anatase-OV. It delivered a reversible capacity of 207.6 mAh g^{-1} at 0.2 C and maintained 115.0 mAh g^{-1} at 10 C, as well as achieved a capacity retention of 99.1% after 500 cycles at 1 C. In line with increasing electronic conductivity and lowering energy barrier of ion diffusion, TiP_2O_7/carbon composite with rich OVs was applied as an anode for both SIBs and PIBs [73]. The content of OVs in TiP_2O_7 was varied by changing the calcination temperature, and the optimised OV content resulted in great electrochemical stability and strong coordination capability with Na^+ and K^+ (Fig. 9c). Surprisingly, despite K^+ has a larger size than Na^+, the anode exhibited comparable rate capability to store the two ions, retaining the capacities of 124.9 and 138.8 mAh g^{-1} at 5 A g^{-1} in SIBs (Fig. 9d) and PIBs (Fig. 9e), respectively. It also exhibited stable long-term cyclability at current density of 1 A g^{-1} by delivering 215.5 mAh g^{-1} after 6000 cycles for SIBs and 177.2 mAh g^{-1} after 5300 cycles for PIBs. It was demonstrated that when using oxygen-deficient $K_{0.8}Mn_8O_{10}$ as a cathode in ZIBs, simultaneous insertion and conversion reaction occurred based on H^+ storage mechanism, leading to a significant energy output of 398 Wh kg^{-1} (based on the mass of cathode) and an impressive durability over 1000 cycles with no obvious capacity fading [92]. OVs not only improved the electronic conductivity of $K_{0.8}Mn_8O_{10}$ but also opened the MnO_6 polyhedron walls for ion diffusion (Fig. 9f), which played a critical role in the fast reaction kinetics and obtained battery performance.

In addition to directly narrowing band gaps, introducing OVs can create defect states, which also leads to the enhancement of electronic conductivity. Yang et al. [113] calculated the DOS of $K_2Ti_6O_{13}$ before and after the introduction of OVs and showed that a defect state was created between 1.5-2.4 eV (Fig. 9g). Since the defect state was closer to the conduction band, it tended to provide electrons and increased the density of carriers, thus improving the electronic conductivity of $K_2Ti_6O_{13}$. This was in accordance with the smaller R_{ct} of oxygen deficient $K_2Ti_6O_{13}$ compared to pristine $K_2Ti_6O_{13}$. As a result, oxygen deficient $K_2Ti_6O_{13}$ showed enhanced electrochemical performance and superior cycling stability in SIBs. It delivered capacities of 249, 239, 224, 194, 168, 136, and 103 mAh g^{-1} at 0.1, 0.2, 0.5, 1, 2, 5 and 20 C, respectively (Fig. 9h), and 90% of the capacity was retained after 20000 cycles at 20 C.

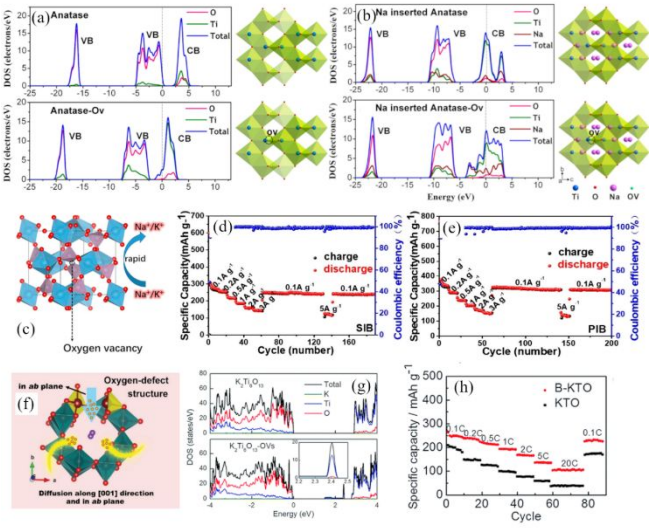

Figure 9. Calculated DOS of (a) anatase and anatase-OV, (b) Na-inserted anatase and Na-inserted anatase-OV. Reproduce with permission [112]. Copyright 2016, American Chemical Society. (c) Schematic image of oxygen deficient TiP_2O_7 structure; rate capabilities of oxygen deficient TiP_2O_7 in (d) SIB and (e) PIB. Reproduce with permission [73]. Copyright 2019, American Chemical Society. (f) Schematic image of oxygen deficient $K_{0.8}Mn_8O_{10}$ structure. Reproduce with permission [92]. Copyright 2019, Wiley-VCH. (g) Calculated DOS and (h) rate capabilities of pristine $K_2Ti_6O_{13}$ and oxygen deficient $K_2Ti_6O_{13}$. Reproduce with permission [113]. Copyright 2018, Royal Society of Chemistry.

4.1.2 Increasing active sites to store ions

OVs can serve as active sites for ion storage during charge and discharge processes, which is beneficial to reach high utilisation of metal oxide electrodes. These active sites have a lower absorption energy of ions due to the introduction of OVs [58]. With the high utilisation of metal oxides, the initial capacity of these oxygen deficient electrodes can be increased. In addition, since the formation of OVs tend to occur at the surface of the electrodes, a high capacitive storage behaviour is often observed, leading to enhanced rate performance [85,114]. Zhang et al. [115] investigated the electrochemical performance of a LIB anode Nb_2O_5, which was treated in a H_2 atmosphere for 10 and 30 minutes (H-Nb_2O_5-10 and H-Nb_2O_5-30, respectively). H-Nb_2O_5-10 (Fig. 10a) exhibited a capacity of 180 mAh g^{-1} at a current density of 0.5 A g^{-1}, largely exceeding pristine Nb_2O_5 (T-Nb_2O_5, 161 mAh g^{-1}). The rate capability of H-Nb_2O_5-10 was also significantly enhanced, with almost 50% initial capacity at a low current density of 0.5 A g^{-1} being kept at a very high current density of 50 A g^{-1}, whereas pristine Nb_2O_5 retained only 15% of the initial capacity at the same current density (Fig. 10b). H-Nb_2O_5-30 delivered lower capacities than pristine Nb_2O_5 at low current densities (< 5 A g^{-1}) but higher capacities were retained at high current densities (> 5 A g^{-1}). The authors claimed that the higher initial capacity of H-Nb_2O_5-10 at a low current density was due to more active sites created by OVs and the lower initial capacity of H-Nb_2O_5-30 was because of the formation of NbO_2 phase at the surface of the material. Moreover, the enhanced rate capability of H-Nb_2O_5-10 and H-Nb_2O_5-30 was largely attributed to the capacitive Li^+ storage due to the introduction of OVs and the resulting improved reaction kinetics. The power law relationship between CV peak currents and scan rates was used to extract the *b* values of the anodic CV peaks of the samples. The value suggested that H-Nb_2O_5-10 and H-Nb_2O_5-30 exhibited a mainly surface controlled Li^+ storage process (*b* = 0.90 and 0.80, respectively), while pristine Nb_2O_5 exhibited a more diffusion-controlled process (*b* = 0.69). Moreover, 75% of the capacity of H-Nb_2O_5-10 was attributed to a capacitive process, and this ratio was further increased to 88% when the scan rate increased from 1 to 5 mV s^{-1} (Fig. 10c). For the case of pristine Nb_2O_5, the capacitive process only occupied 53% and 72% of the total capacity at 1 and 5 mV s^{-1}, respectively. Similar results were observed in a study of oxygen deficient MoO_3 (Fig. 10d) as a LIB anode material [31]. It delivered a capacity of 222 mAh g^{-1} at a scan rate of 10 mV s^{-1}, which was much higher than that of pristine MoO_3 (153 mAh g^{-1}). CV results (Fig. 10e) showed that the *b* value of oxygen deficient MoO_3 was 1, suggesting the capacitor-like nature of the reaction kinetics. In contrast, the *b* value of pristine MoO_3 was 0.7, indicating the diffusion-controlled reaction kinetics. This was further verified by the quantitatively calculations of capacitive contribution. 75% of the total capacity of oxygen deficient MoO_3 was contributed by a capacitive process (Fig. 10f), which was a much greater number than that of pristine MoO_3 (37%).

Divalent ions such as Zn^{2+} have a higher charge density (charge/size ratio) than monovalent ions and a higher compulsive force with oxygen anions in the host structure. The diffusion of divalent ions can cause the structural deformation of host lattices and sometimes even electrochemical inactivity; hence, the utilisation of OVs is of particular interest for divalent-ion batteries. Oxygen deficient Mn_3O_4 (Fig. 10g) was synthesised in an alkaline solution (pH = 10.5) that enables a rapid nucleation and growth of nanoparticles [116], resulting in abundant OVs on the surface of the nanoparticles, which was evidenced by the higher Mn^{2+}/Mn^{4+} ratio (4:1) than that of stoichiometric Mn_3O_4 (2:1).

The OVs on the exposed surface of the nanoparticles not only enable a high D_{Zn} of 2.4×10^{-10} cm^2 s^{-1}, which was more than two orders of magnitude higher than that of other spinel oxide cathode for Zn-ion batteries [117,118], but also act as active sites for electrochemical reactions. A capacitive process played a major role in the capacity contribution to Zn^{2+} storage, being estimated to be > 70% at high scan rates (Fig. 10h). As a result, the oxygen deficient Mn_3O_4 cathode delivered very high capacities of 386.7, 336.2, 284.4, 245.7, 182.3, 158.3 and 121.6 mAh g^{-1} at current densities of 0.1, 0.2, 0.4, 0.6, 0.8, 1.0 and 1.5 A g^{-1}, respectively (Fig. 10i). DFT calculations carried out on oxygen deficient Co_3O_4 by Lu et al. [58] showed that the adsorption energy for the Co_3O_4 surface with one OV was lower than that of the OV-free surface (-4.44 vs. -2.97 eV). This evidenced that OVs could act as active sites to promote the adsorption of OH^- onto the Co_3O_4 surface, which was crucial for the reactivity of Co_3O_4 in ZIBs, as OH^- took part in the redox reaction of Co_3O_4 to store Zn^{2+}.

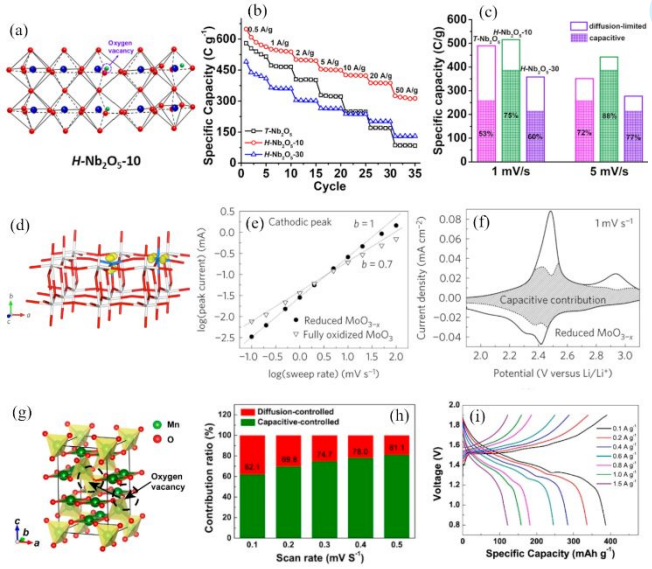

Figure 10. (a) Schematic image of H-Nb_2O_5-10 structure; (b) rate capability and (c) contribution ratio of capacitive and diffusion-controlled capacities at 1 mV s^{-1} and 5 mV s^{-1} of different Nb_2O_5 samples. Reproduce with permission [115]. Copyright 2020, Elsevier. (d) Schematic image of oxygen deficient MoO_3 structure; (e) the log(i) versus log(v) plot of the cathodic current response at ~2.4 V (versus Li/Li$^+$); (f) contribution of capacitive-controlled capacity of oxygen deficient MoO_3. Reproduce with permission [31]. Copyright 2017, Springer Nature. (g) Schematic image of oxygen deficient Mn_3O_4 structure; (h) contribution ratio of capacitive and diffusion-controlled capacities at different scan rates of oxygen deficient Mn_3O_4; (i) charge/discharge profiles of oxygen deficient Mn_3O_4 at different current densities. Reproduce with permission [116]. Copyright 2019, American Chemical Society.

4.1.3 Inducing built-in electric field

Unbalanced charge distribution can appear around the sites of OVs and lead to the formation of local built-in electric field, which could facilitate ion transfer [40,119,120]. As shown in Fig. 11a, the presence of an OV in the material induces a lopsided charge distribution to emerge, which leads to a positive area in the OV site and an equivalent negative area around the OV due to the excess electrons, hence resulting in a built-in electric field [121]. During the discharging process, the electric field points from the defect free area to the negatively charged area around the OV, which accelerates the inward transfer of Li^+, so the coulombic force would gather the ions around the OV site. The negatively charged area tends to become electrically neutral after a lithiation process. During the charging process, the electric field points from the positively charged OV site to the electrically neutral lithiation layer, which facilitates the outward transfer of Li^+ and promote the Li^+ extraction process. Chen et al. carried out a DFT study to investigate the OV-induced built-in electric field in detail by taking TiO_2 as an example [122]. Excess electrons are created by OVs, and these electrons are localised near Ti atoms. These excess electrons can be regarded as negative charge centres to trap positively charged alkaline ions. The location of the excess electrons changes as the movement of Li^+, depending on the electrostatic interaction between the ions and the excess electrons. The energy barrier for Li^+ transfer from one stable site to another in the OV-free TiO_2 was calculated to be 0.63 eV (Fig. 11b). In contrast, the energy barrier in TiO_2 with one OV was 0.53 eV (Fig. 11c), suggesting easier ion diffusion in TiO_2 with OVs. The facilitation of Li^+ migration was experimentally supported by the diffusion coefficient (D_{Li}) of oxygen deficient TiO_2 (2.99×10^{-9} cm^2 s^{-1}), which was two orders of magnitude higher than that of pristine TiO_2 (1.45×10^{-11} cm^2 s^{-1}). Oxygen deficient TiO_2 delivered a capacity of 290.0 mAh g^{-1} at 0.5 C and retained 192.5 mAh

g^{-1} at 10 C. The effect of unbalanced charge distribution caused by OVs on ion transfer has also been reported in divalent ion batteries.

It is worth noting that although built-in electric field induced by OVs can facilitate ion migration, it is not always the case when there is a high concentration of OVs. As shown by the afore-mentioned work of TiO_2 [122], when the number of OVs was doubled, the calculated energy barrier of Li^+ migration was 1.17 eV (Fig. 11d), which was even higher than that of OV-free TiO_2. This is because a high OV concentration leads to a large number of excess electrons, which depletes free Li^+ due to its association of the excess electrons. Therefore, well-balanced numbers of lithium ions and excess electrons are essential to facilitate lithium ion diffusion [43]. A volcano correlation between OV concentration and battery performance has been seen in the previous work [53,123]. Oxygen deficient MoO_{3-x} exhibited a nearly theoretical capacity as a LIB anode when x = 0.03, as compared to 0 and 0.5 [53]. Oxygen deficient Li_3VO_4 with a V^{4+}/V^{5+} molar ratio of 0.08 exhibited a higher D_{Li} and better electrochemical performance than the counterparts with the ratios of 0.05, 0.09 and 0.10 [123].

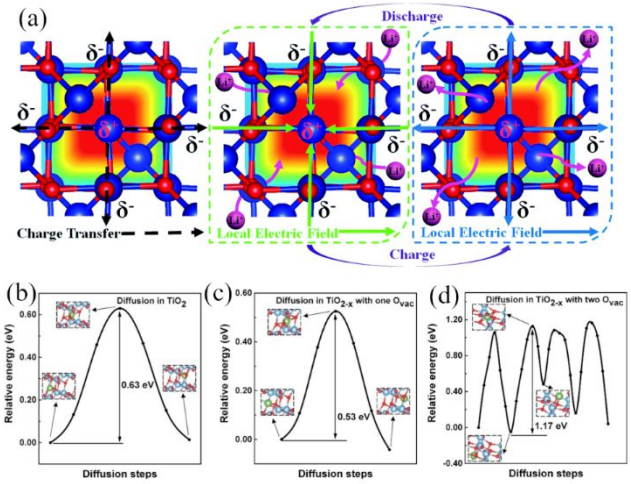

Figure 11. (a) Schematic image of the oxygen vacancy derived local built-in electric field. Reproduce with permission [121]. Copyright 2018, Royal Society of Chemistry. (b)(c)(d) The energy barrier of Li^+ migration along the diffusion pathway for perfect TiO_2, TiO_{2-x} with one OV and TiO_{2-x} with two neighbouring OVs. Reproduce with permission [122]. Copyright 2020, Wiley-VCH.

4.1.4 Causing phase change

The presence of OVs can cause phase change of electrode materials and as a result, change the reaction mechanisms of the materials. This has often been observed in conventional cathodes with a layered or spinel structure. The phase change not only suppresses the irreversible oxygen extraction during a charge process and activates transition metal redox site, but also introduces new electrochemically active phases that can offer an extra capacity [4,124]. Kubota et al. first discovered that the reaction mechanism of a Li-rich layered cathode Li_2MnO_3 changed after the introduction of OVs [55]. They reported that pristine Li_2MnO_3 exhibited a long plateau at 4.5 V in the first charge process, and no plateau in the following cycles (Fig. 12a), whereas oxygen deficient Li_2MnO_3 exhibited no plateau at 4.5 V in the first charge process but two plateaus at 3.2 V and 4.0 V in the following cycles (Fig. 12b). The authors attributed the long plateau at 4.5 V and above to the irreversible oxidation of O^{2-} into a higher valence state, such as oxygen gas or O_2^-, and Mn remained at the +4 state during the first charge but became electrochemically active during the first discharge. DFT calculations [125] suggested that OVs can suppress the oxidation of O^{2-} and activate the Mn redox site, resulting in the absence of the plateau at 4.5 V. This is because during lithium extraction, compared to pristine Li_2MnO_3, a larger number of electrons were withdrawn from the Mn *d* orbitals of oxygen deficient Li_2MnO_3 and the charge variation of Mn was increased, therefore the average net charge of O atom was lowered. It was then reported by Sun et al. that $LiMnO_2$ phase was detected in oxygen deficient Li_2MnO_3 by XRD patterns [126], where several additional diffraction peaks in the XRD pattern (Fig. 12c) were indexed to the $LiMnO_2$ phase. According to the Rietveld analysis results, oxygen deficient Li_2MnO_3 synthesised by the authors consisted of 71.45% of Li_2MnO_3 phase and 28.55% of $LiMnO_2$ phase. The authors observed the characteristic plateau of oxidisation of O^{2-} at 4.7 V in the first charge process of pristine Li_2MnO_3. For oxygen deficient Li_2MnO_3, the redox pair at 4.1/3.9 V

was assigned to the phase transformation between $LiMnO_2$ and a spinel-like structure, and the one at 3.4/3.0 V corresponded to lithium extraction and insertion from/to $LiMnO_2$ (Fig. 12d) [77,126]. With the generation of OVs, the electrochemical performance of the oxygen deficient Li_2MnO_3 was greatly enhanced. It exhibited a capacity of 225.7 mAh g^{-1} at 20 mA g^{-1}, which was much higher than that of pristine Li_2MnO_3 (about 76 mAh g^{-1}) at the same current density (Fig. 12d). The Coulombic efficiency (CE) of the oxygen deficient Li_2MnO_3 was also increased due to the suppression of the irreversible oxygen oxidation. It is worth noting that, for Li-Mn-O spinel cathode, the phase change caused by oxygen vacancies can cause disadvantage. According to Yoshio et al., oxygen deficient $LiMn_2O_4$ undergoes a phase change from cubic to tetragonal at room temperature. The formed tetragonal $Li_2Mn_2O_4$ phase was difficult to be charged, leading to severe capacity fade [127].

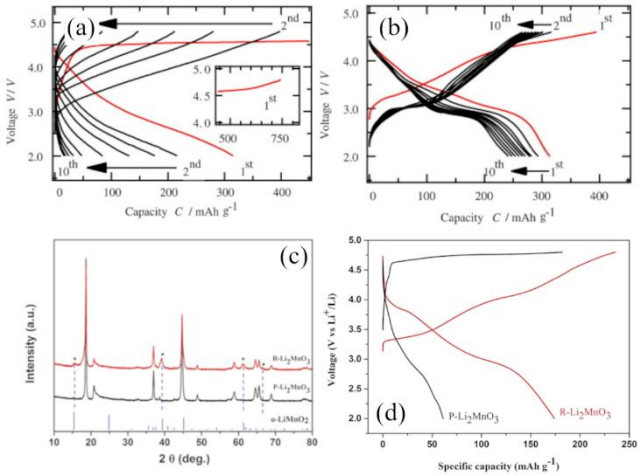

Figure 12. Charge/discharge profile of (a) Li_2MnO_3 and (b) oxygen deficient Li_2MnO_3 at 10 mA g^{-1}. Reproduce with permission [55]. Copyright 2012, Elsevier. (c) XRD patterns of oxygen deficient Li_2MnO_3; (d) charge/discharge profile of pristine Li_2MnO_3 and oxygen deficient Li_2MnO_3. Reproduce with permission [77]. Copyright 2019, Elsevier.

Another example for Li-rich layered cathode material was $Li_{1.2}Mn_{0.54}Ni_{0.13}Co_{0.13}O_2$ (LMNC), which is based on the Li_2MnO_3-$LiMO_2$ (M=Mn, Ni, Co) system. Cai et al. [128] reported that a thin layer (10-20 nm) of spinel phase ($Li_4Mn_5O_{12}$) was formed on the surface of oxygen deficient LMNC, due to the generation of OVs. The presence of *Fd-3m* $Li_4Mn_5O_{12}$ phase was confirmed by HRTEM and XRD (Fig. 13a). According to the Rietveld refinement analysis, the amount of the $Li_4Mn_5O_{12}$ phase accounted for 3.7 wt.%. The spinel layer was dual functional. First, it has 3D diffusion channels which can facilitate Li^+ transfer between the electrolyte and the layered LMNC, leading to an enhancement of Li^+ diffusion coefficient from 3.62×10^{-18} to 4.58×10^{-16} cm^2 s^{-1}. The oxygen deficient LMNC delivered reversible capacities of 290, 283, 275, 249 and 221 mAh g^{-1} at 0.2, 0.5, 1, 5 and 10 C, respectively, whereas those of pristine LMNC were 285, 273, 257, 202 and 170 mAh g^{-1} (Fig. 13b). Second, the spinel layer can largely suppress the formation of solid electrolyte interface (SEI) layer and enhance the structural stability of the oxygen deficient LMNC. It exhibited a very high initial CE of 92.3%, and the small discharge plateau at 2.8 V for oxygen deficient LMNC was ascribed to spinel discharge process (Fig. 13c). Capacity retentions of 95.7% and 91.6% were achieved after 100 cycles at 2500 and 5000 mA g^{-1}, respectively. $LiNi_{0.5}Mn_{1.5}O_2$ (LNMO) is a spinel cathode material and exhibits two different spinel phases, ordered phase (*$P4_332$*) and disordered phase (*Fd3m*). All Mn ions are at +4 state in ordered LNMO, while a small amount of Mn ions is +3 state in disordered LNMO [129]. The structural orderliness of LNMO is determined by the arrangement of Ni/Mn and it is closely related to oxygen deficiency and the concentration of Mn^{3+} [130-131]. According to the DFT calculations, the formation energy of *$P4_332$* phase is 0.76 eV lower than that of the *Fd3m* phase. However, because of the generation of OVs and the reduction of the Mn ions adjacent to OVs from +4 state to +3 state, the energy difference between the two phases decreases from 0.76 to 0.21 eV and even -0.44 eV, indicating that the dominance of the *$P4_332$* phase in stoichiometric LNMO is lifted and the *Fd3m* phase is even more thermodynamically preferred [130]. According to the SAED patterns, LMNO with a higher OV concentration exhibited a pure *Fd3m* diffraction pattern (Fig. 13d), while LMNO with lower OV concentration exhibited both *$P4_332$*

and *Fd3m* diffraction pattern (Fig. 13e) [131]. Liu et al. synthesised LNMO with various amounts of OVs and verified the correlation of Ni/Mn disordering and OVs [132]. A high amount of OVs led to a high degree of Ni/Mn disordering, which resulted in the dominance of the *Fd3m* phase (> 97%), while a low amount of OVs led to pure $P4_332$ phase. The disordered phase exhibited an electronic conductivity of ~1×10^{-6} S cm^{-1}, being two orders of magnitude higher than that of the ordered phase (1.9×10^{-8} S cm^{-1}). Disordered phase-dominated LNMO-O_2, LNMO-N and LNMO-5 exhibited a similarly high capacity retention of ~95% after 500 cycles at 73.5 mA g^{-1} (Fig. 13f), which was much higher than those of the mixed-phase LNMO-1 and LNMO-A (~80%). This improvement was even more significant when the temperature was elevated to 60˚C, i.e., 72~81% capacity retention for LNMO-O_2, LNMO-N and LNMO-5 and only 15% for LNMO-A.

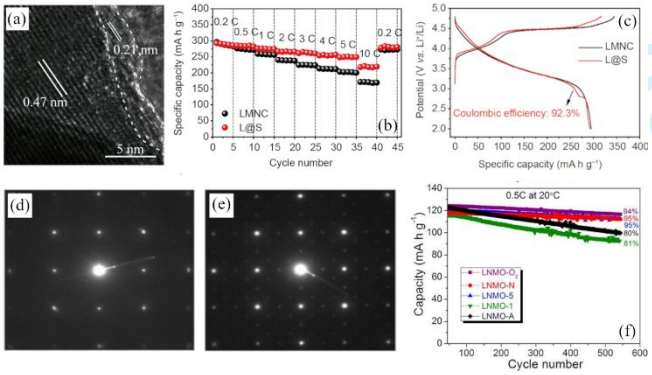

Figure 13. (a) HRTEM of oxygen deficient LMNC; (b) rate capability and (c) charge/discharge profile of pristine LMNC and oxygen deficient LMNC. Reproduce with permission [128]. Copyright 2019, Springer Nature. Electron diffraction patterns of (d) LMNO with a higher OV concentration and (e) LMNO with a lower OV concentration. Reproduce with permission [131]. Copyright 2012, Wiley-VCH. (f) Cycling performance of LNMO with various amounts of OVs. Reproduce with permission [132]. Copyright 2018, Springer Nature.

Besides altering phase change of layered cathodes, OVs can also facilitate phase change during cycling. An interesting example was reported by Jiang et al. for SIBs [133]. In-situ XRD (Fig. 14) was used to monitor the phase change during the first cycle of pristine $Na_{0.9}Ni_{0.3}Co_{0.15}Mn_{0.05}Ti_{0.5}O_2$ (NaNCMT-2) and oxygen deficient $Na_{0.9}Ni_{0.3}Co_{0.15}Mn_{0.05}Ti_{0.5}O_2$ (NaNCMT-1). When NaNCMT-2 was first charged to 4.0 V, the phase change from pure O3 to the coexistence of O3/P3 and further to pure P3 was clearly observed. However, during the discharging process to 2.0 V, NaNCMT-2 was not able to evolve back to pure O3 and kept the existence of O3 and P3. This irreversible phase change led to a very poor initial CE of 65.7% with a discharge capacity of 86.9 mAh g^{-1}. In contrast, NaNCMT-1 exhibited a full reversible phase transition between O3 and P3 in the voltage range of 2.0–4.0 V. The reversibility led to a high initial CE of 97.3% with a discharge capacity of 112.7 mAh g^{-1}. The authors explained that the abundant OVs in the sample lowered the phase transition energy barrier between O3 and P3 phases and as a result boosted reversible Na (de)intercalation.

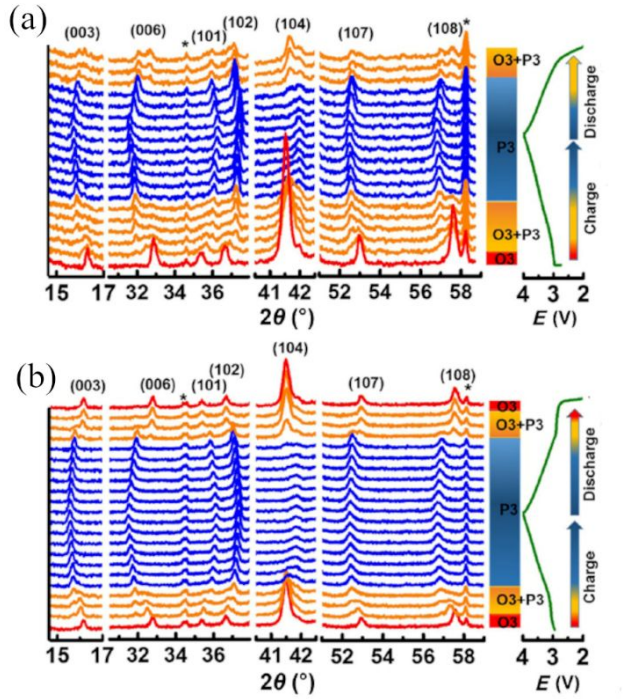

Figure 14. In-situ XRD patterns of (a) NaNCMT-2 and (b) NaNCMT-1 electrodes during first cycle at 0.2 C. Reproduce with permission [133]. Copyright 2021, Springer Nature.

4.2 The role of OVs in metal oxides as coating layers

Unlike the effects discussed in the last section where oxides with OVs are directly applied as electrode materials, oxides with OVs can benefit electrode materials indirectly as coating layers during charge and discharge processes. In other words, oxygen deficient metal oxides are not electrochemically active within the operating voltage window, but they act as a coating layer outside the active electrode materials. Chen et al. coated a layer of oxygen deficient SnO_2 on the surface of a Li-rich layered cathode material, $Li_{1.2}Mn_{0.54}Ni_{0.13}Co_{0.13}O_2$ (LMNC) [134]. Two significant differences in electrochemical performance were observed between the

coated and uncoated LMNC. First, the initial charge and discharge capacities were increased by about 40 mAh g^{-1} after coating, and the charge capacity increase was attributed to the longer plateau at 4.5 V (Fig. 15c). As previously discussed, the redox reaction of Li_2MnO_3 at 4.5 V or even a higher potential represents the irreversible oxidisation of O^{2-} to the oxygen species with higher valence states, such as O or O_2^-. They transfer to the surface of the electrode to either form oxygen gas or react with electrolyte causing severe oxygen loss. The OVs in the SnO_2 coating layer can receive the oxygen species with higher valence states and facilitate the oxygen transfer to the coating layer during the activation of Li_2MnO_3 (Fig. 15a). Therefore, the oxygen deficient SnO_2 layer can promote the activation of Li_2MnO_3 component in LMNC and improve the initial charge capacity. The more activated Li_2MnO_3 component in the coated LMNC also led to a higher initial discharge capacity. Second, the cycling stability of the coated LMNC was largely improved (Fig. 15d), showing a capacity retention of 89.9% after 200 cycles at 300 mA g^{-1}. In contrast, 78.5% of the initial capacity of the pristine LMNC was remained after 200 cycles. Since oxygen loss was suppressed because of the OVs in the SnO_2 coating, a thin and stable SEI layer was formed, which improves the Li^+ transfer in comparison to the thick and compact SEI layer outside the pristine LMNC. This was verified by the largely decreased surface film resistance (R_{sf}) and charge transfer resistance (R_{ct}) of the coated LMNC (19.25 and 8.527 Ω respectively), compared to the pristine LMNC (35.34 and 184.3 Ω, respectively). The improved cycling stability was also benefited from the coating layer which protected the material from the erosion of HF caused by the decomposition of the electrolyte. Beside SnO_2, oxygen deficient MoO_3 [135] and CeO_2 [136] were also coated on the surface of LMNC. It was essential that the amount of the coating layer needs to be optimised, e.g., 3 wt% for MoO_3 and 4 wt% for CeO_2, to achieve the best battery performance of LMNC. Furthermore, it was observed that a small amount of spinel phase was formed at the interphase between LMNC and the oxygen deficient coating layer (Fig. 15b), which was attributed to the H^+/Li^+ ion exchange reaction due to the hydrolysis of the precursor of the coating material, meaning Li^+ was pre-extracted during the surface coating process to form a more stable spinel phase. The spinel phase has 3D channels for Li^+ diffusion, hence facilitating the ions to transfer between electrolyte and LMNC. Benefiting from the spinel phase and the thin and stable SEI layer, all the LMNC samples with oxygen deficient CeO_2 layer exhibited lower R_{sf} and R_{ct} than the pristine LMNC (Fig. 15e). This reduced resistance further led to better rate capability of the coated LMNC (Fig. 15f). LMNC with optimised oxygen deficient CeO_2 layer provided the best rate capability with very little capacity decay when the current density was increased from 0.1 to 0.5 C. A capacity of 186.5 mAh g^{-1} was achieved at 5 C compared with only 164.3 mAh g^{-1} for pristine LMNC [136]. Du et al. reported a TiO_{2-x} coated $Na_3V_2O_2(PO_4)_2F$ SIB cathode material [137]. The OVs in the TiO_{2-x} coating layer increased D_{Na} from 1.157×10^{-15} to 2.341×10^{-15} cm^2 s^{-1}. The TiO_{2-x} layer also protected the electrode material from direct contact with the electrolyte, leading to hindered side reaction and a thin and stable SEI layer, which resulted in decreased charge transfer resistance from 398 to 310 Ω. TiO_{2-x} coated $Na_3V_2O_2(PO_4)_2F$, with the optimised coating amount of 3 wt%, delivered a reversible capacity of 100 mAh g^{-1} after 100 cycles at 25.6 mA g^{-1} and retained 85% of the initial capacity (Fig. 15h), which was greatly higher than that of pristine $Na_3V_2O_2(PO_4)_2F$ (~70%). Although TiO_2 did not offer capacity in the cathode potential range, the capacity did increase by ~20 mAh g^{-1} due to the reduced resistance and the enhanced D_{Na} (Fig. 15g).

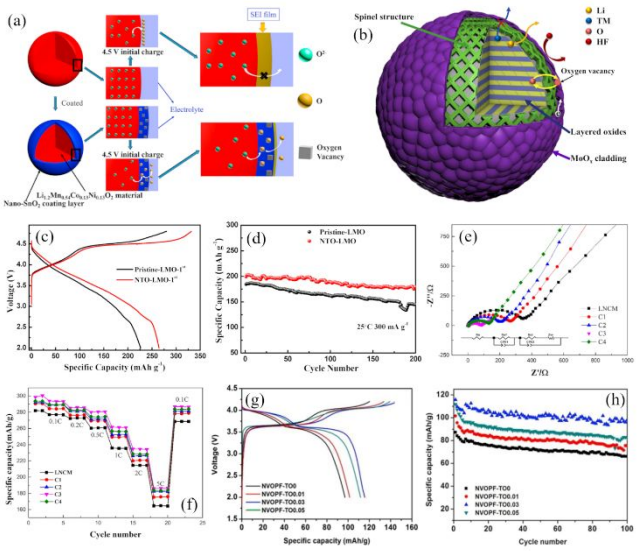

Figure 15. (a) Schematic image of the mechanism of OVs in SnO_2 coating layer on the Li-rich oxide material. Reproduce with permission [134]. Copyright 2016, Elsevier. (b) Schematic image of the spinel phase between LMNC and the oxygen deficient coating layer. Reproduce with permission [135]. Copyright 2019, Elsevier. (c) Charge/discharge profile and (d) cycling performance of pristine LMNC and coated LMNC. Reproduce with permission [136]. Copyright 2018, Springer Nature. (g) Charge/discharge profile and (h) cycling performance of NVOPF with different amount of coating layer. Reproduce with permission [137]. Copyright 2020, Elsevier.

4.3 The synergistic role of OVs with other contributors

4.3.1 Interplay between OVs and carbonaceous materials

Carbon as the most common and effective conductive additive can be incorporated with OV-containing metal oxides to boost their electrochemical performance by improving charge transfer properties, due to the conductive nature of carbon and the accelerated redox reaction kinetics [138-140]. In general, carbon could be incorporated either by the carbonisation of organic precursors or residual organic additives during the formation of OVs or via the post treatment of OV-containing oxides. Yang et al. fabricated carbon coated (thickness: 2nm) oxygen deficient MoO_3 (Fig. 16a) as an anode for LIBs and compared its electrochemical properties with the uncoated counterparts [57]. The electrochemical impedance spectroscopy (EIS) results showed that R_{ct} significantly decreased from 1721.4 to 844.9 Ω after generating OVs in MoO_3 (Fig. 16b). The carbon coating layer further reduced the resistance to 505.9 Ω, indicating that OVs had a positive effect on electronic conductivity, and carbon further facilitated the charge transfer. The calculated D_{Li} exhibited a similar trend, being 1.46×10^{-12}, 4.50×10^{-11} and 7.14×10^{-11} cm^2 s^{-1} for pristine MoO_3, MoO_{3-x} and carbon coated MoO_{3-x}, respectively. Owing to the improvement of electronic and ionic conductivity, carbon coated MoO_{3-x} exhibited enhanced rate capability, delivering higher capacities of 1005, 980, 890, 830, 650, 505 mAh g^{-1} at 0.1, 0.2, 0.5, 1, 2 and 5 A g^{-1}, respectively (Fig. 16c). Gan et al. compared pristine TiO_2 (TO), TiO_2 with OVs (DTO), TiO_2 with N-doped carbon layer (NC-TO) and TiO_2 with both OVs and N-doped carbon layer (NC-DTO, Fig. 16d, discontinued lattice fringes indicated by red circles suggesting the presence of OVs), and they concluded that the combination of OVs and carbon coating achieved the best electrochemical performance [141]. Despite either OVs or carbon layer was able to enhance the electronic conductivity of TiO_2 by four orders of magnitude, from 3.3×10^{-8} to ~10^{-4} S cm^{-1}, NC-DTO exhibited the highest value of 1.7×10^{-3} S cm^{-1}. In addition, NC-DTO had the lowest R_{ct} and the highest D_{Na} among the four samples (Fig. 16e). The synergistic effect of OVs and carbon layer resulted in the highest reversible capacities of 170 and 150 mAh g^{-1} at 10 and 15 C, respectively (Fig. 16f). The effect of carbon additives on cycling stability is even more crucial for OV-containing metal oxides that undergo a conversion and/or an alloying reaction to store ions. SnO_2 is regarded as a typical example and struggles with large volume change and poor reversibility during cycling [30,142]. Ma et al. fabricated a composite of oxygen deficient SnO_2 and carbon nanofibres, where the former was impregnated to the latter using a well-controlled electrospinning technique [143]. During the discharge process of pristine SnO_2, Sn and Na_2O tended to self-aggregate and separate from each other, and Na_2O separated from the Na_xSn/Na_2O interface because of the huge volume change associated with the alloying reaction. Therefore, the structure of SnO_2 destructed, resulting in a

rapid capacity decay. In contrast, carbon fibres can not only effectively prevent the aggregation and separation of Sn and Na_2O, but also alleviate the stress derived from the volume expansion as SnO_2 was well-distributed in the carbon fibres, which led to superior cycling stability (Fig. 16g). Oxygen deficient SnO_2 confined in carbon nanofibres retained a reversible capacity of ~600 mAh g^{-1} after 2000 cycles at 1 A g^{-1}, whereas pristine SnO_2 practically failed after only 800 cycles at the same current density (Fig. 16h).

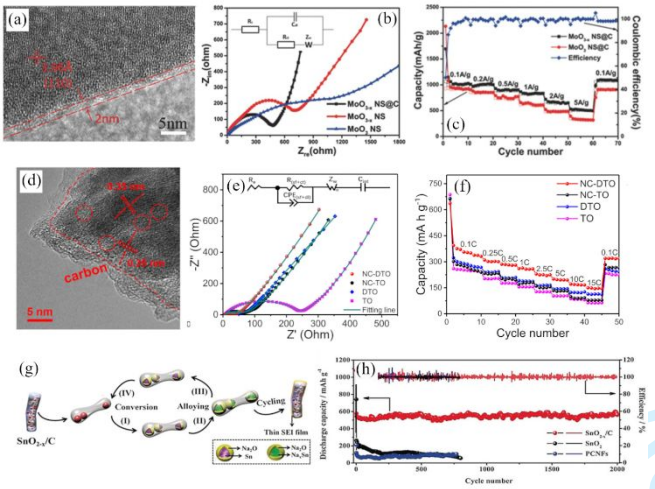

Figure 16. (a) TEM image of oxygen deficient MoO_3; (b) EIS results and (c) rate capability of pristine MoO_3, MoO_{3-x} and carbon coated MoO_{3-x}. Reproduce with permission [57]. Copyright 2016, Wiley-VCH. (d) TEM image of N-doped carbon coated oxygen deficient TiO_2; (e) EIS results and (f) rate capability of pristine TiO_2, TiO_2 with OVs, TiO_2 with N-doped carbon layer and TiO_2 with both OVs and N-doped carbon layer. Reproduce with permission [141]. Copyright 2018, American Chemical Society. (g) Schematic image of the reaction mechanism of carbon coated oxygen deficient SnO_2; (h) cycling performance of pristine SnO_2 and carbon coated oxygen deficient SnO_2. Reproduce with permission [143]. Copyright 2018, Wiley-VCH.

Reduced graphene oxide (rGO) has been used as another common and effective carbonaceous additive to enhance the performance of metal oxide electrodes, due to the features of ultrathin two-dimensional structure, excellent electronic conductivity, high surface areas, good mechanical and chemical stability [85,144,145]. Unlike non-graphitic carbon that is obtained via carbonisation, rGO is formed by reducing graphene oxide (GO) and directly introduced to the reaction environment of an active material, where the material and rGO are assembled via chemical bonding or electrostatic attraction [44,85,145,146]. Meng et al. fabricated oxygen deficient $Li_4Ti_5O_{12}$ (LTO) encapsulated in rGO sheets (CT-rGO@LTO) as an anode for LIBs [146]. According to the EIS results, R_{ct} of pristine LTO was largely decreased from ~140 to 38 Ω due to the benefits of OVs and rGO. CT-rGO@LTO showed a higher D_{Li} than pristine LTO (2.9×10^{-10} vs. 4.1×10^{-11} cm^2 s^{-1}). Moreover, the presence of rGO alleviated the agglomeration of LTO during the calcination process, resulting in an increased surface area from 3.1 to 82.9 m^2 g^{-1} and a reduced migration path for Li^+. With the boosted reaction kinetics, CT-rGO@LTO exhibited improved rate capability, delivering the specific capacities of 168.6, 160.4, 156.2, 146.5, 138.0, 128.3, 116.6 and 101.1 mAh g^{-1} at 0.2, 0.5, 1, 3, 5, 10, 20 and 40 C, respectively (Fig. 17a). CT-rGO@LTO also exhibited a capacity retention of 94.9% after 600 cycles at 175 mA g^{-1} (Fig. 17b), which was superior to pristine LTO (86.1% after 500 cycles). Another worth mentioning work was provided by Wu et al. who investigated the synergistic effect of OVs and N-doped rGO by comparing pristine SnO_2, SnO_2 with carbon coating (SnO_2/C) and SnO_2 with OVs and N-doped rGO (SnO_2/N-rGO) [147]. Carbon coating reduced R_{ct} of pristine SnO_2 from 534.4 to 124.6 Ω, but OVs and N-rGO further reduced it to 55.7 Ω. As a result, SnO_2/C exhibited better rate capability than pristine SnO_2 only at low to medium current rates (0.2-1 A g^{-1}), while SnO_2/N-rGO exhibited significantly improved rate capability at high rates (> 1 A g^{-1}), with stable capacities of 434, 371 and 309 mA h g^{-1} at 2, 5, and 10 A g^{-1}, respectively (Fig. 17c). In addition, SnO_2/N-rGO also exhibited the best cycling stability among the three samples (Fig. 17d). Pristine SnO_2 and SnO_2/C only maintained 27 and 110 mAh g^{-1}, respectively, after 500 cycles at 0.5 A g^{-1}, while SnO_2/N-rGO still maintained a decent capacity of 912 mAh g^{-1}. The authors attributed the results to the rGO entrapped structure because the separation and aggregation of Sn and Li_2O were prevented and the volume expansion stress was largely alleviated, enabling reversible conversion and alloying process during cycles.

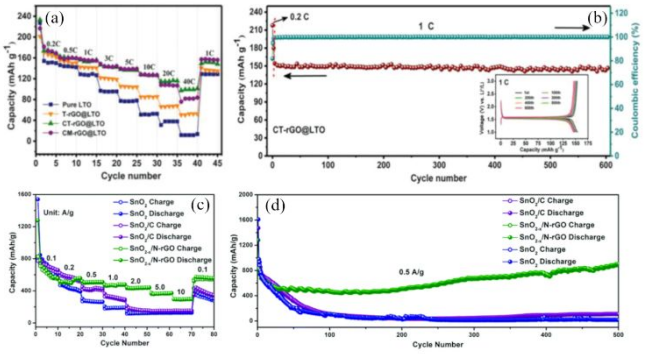

Figure 17. (a) Rate capability and (b) cycling performance of rGO encapsulated oxygen deficient $Li_4Ti_5O_{12}$. Reproduce with permission [146]. Copyright 2019, Wiley-VCH. (c) Rate capability and (d) cycling performance of pristine SnO_2, SnO_2 with carbon coating and SnO_2 with OVs and N-doped rGO. Reproduce with permission [147]. Copyright 2018, Royal Society of Chemistry.

4.3.2 Interplay between OVs and doping

Doping metal oxides with foreign elementals can create OVs and improve the electrochemical performance of metal oxides. The direct benefit derived from dopants have been widely studied and understood as well as discussed in previous sections. What has not been often discussed is the synergistic effect of dopants and OVs, and the synergistic effect can have a profound impact on the properties of metal oxides [148]. On the one hand, the electronic structure of metal oxides is changed due to the dopants and OVs. Wang et al. calculated the DOS of N-doped TiO_2 and found that in addition to the delocalisation of Ti 3d state by OVs, N doping introduced N 2p state slightly above the valence band [149]. When both OVs and N doping were introduced into TiO_2, not only was a dopant energy level formed, but the Fermi level was shifted to the conduction band (Fig. 18a and 18b). As a result, the synergistic effect of OVs and N-doping dramatically increased the electronic conductivity of TiO_2 from 2.4×10^{-8} to 3.33×10^{-5} S cm^{-1} and greatly reduced R_{ct} from 797.2 to 250.4 Ω. N-doped TiO_{2-x} exhibited an improved rate capability compared to pristine TiO_2, with an initial capacity of 265.6 mAh g^{-1} at 50 mA g^{-1} , and 147.9 mAh g^{-1} was still remained at a high current rate of 1 A g^{-1} (Fig. 18c). Similar results were observed from metallic doping for the case of Cu-doped TiO_2 [150]. A dopant energy level was formed at near Fermi level, suggesting a deep donor level and leading to enhanced electron transfer (Fig. 18d). The Na^+ diffusion barrier and R_{ct} of Cu-doped TiO_2 were much lower than those of pristine TiO_2 (0.11 vs. 0.44 eV and 520.4 vs. 759.0 Ω). On the other hand, dopants could introduce new phases to oxygen deficient metal oxides. Metal Cu nanodots with a diameter of 3-5 nm were observed in Cu-doped TiO_2 (Fig. 18e and 18f). The authors claimed that these well-dispersed Cu nanodots acted as conductive connections between TiO_2 particles to facilitate the charge transfer. He et al. reported that a new phase with a lattice fringe of 0.10 nm was observed in N-doped TiO_2 and they referred the phase as $TiO_{2-x}N_y$ (Fig. 18g and 178) [83]. $TiO_{2-x}N_y$ was believed to have positive effect on the electronic conductivity and suppress the agglomeration of TiO_2, as evidenced by the improved battery performance. It is worth noting that the formation of new phases as a result of doping metal oxides might not be initially expected , and in-depth investigations are needed to fully characterise and understand the effects of the newly formed phases on battery performance, in particular how the phases interact and/or affect the presence and evolution of OVs in metal oxides during battery operation.

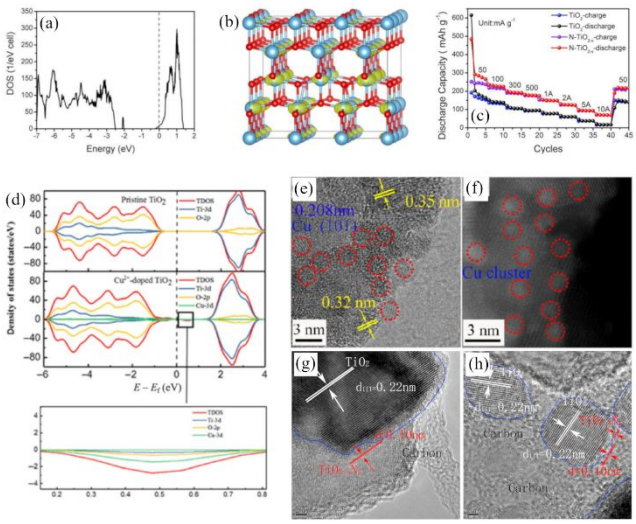

Figure 18. (a) The densities of states and (b) the schematic image of TiO_2 with both OVs and D-doping; (c) rate capability of pristine TiO_2 and N-doped TiO_2. Reproduce with permission [149]. Copyright 2019, Elsevier. (d) The densities of states of pristine TiO_2 and Cu-doped TiO_2; (e) HRTEM and (f) HAADF-STEM image of Cu-doped TiO_2. Reproduce with permission [150]. Copyright 2019, Springer Nature. (g) TEM and (h) HRTEM image of N-doped TiO_2. Reproduce with permission [83]. Copyright 2017, Elsevier.

Oxygen deficient metal oxides are often tested as electrode materials at the as-prepared condition, meaning shortly after OVs are created, and hence it tends to be neglected that dopant might stabilise the presence of OVs in metal oxides. Song et al. compared the performance of Mo-doped OV-containing $Li_4Ti_5O_{12}$ (Mo-LTO-R) and non-doped OV-containing $Li_4Ti_5O_{12}$ (LTO-R) at the as-prepared condition and five weeks after the samples were prepared [86]. The results (Fig. 19a) showed that the performance of LTO-R greatly deteriorated after five weeks, especially at high rates (28% capacity drop at 5 C and 33% at 10 C); however, Mo-LTO-R maintained the performance obtained at the as-prepared condition. The electronic conductivity measurement revealed that it decreased from 8.1×10^{-6} (as-prepared) to $< 10^{-13}$ S cm^{-1} after five weeks for the case of LTO-R, which was only comparable to that of pristine LTO (LTO-O). In contrast, the electronic conductivity of Mo-LTO-R remained at 1.1×10^{-2} S cm^{-1}, suggesting that OVs were stabilised in air by the Mo doping. The authors further investigated the stabilisation mechanism through Ti 2p XPS spectra (Fig. 19b). LTO-O exhibited a single signal of Ti^{4+} and LTO-R exhibited two split signals of Ti^{3+} and Ti^{4+}. Interestingly, Mo-LTO-R exhibited a single signal at an intermediate binding energy between Ti^{3+} and Ti^{4+}. This indicates that Mo doping led to electron delocalisation over the entire lattice, which is clearly different from the locally discrete Ti^{4+}/Ti^{3+} oxidation state change caused solely by the presence of OVs. For LTO-R, the extra charge was only localised near the OV sites, and such localised charge distribution is unstable, resulting in the deterioration of the electronic conductivity with time and eventually reached a similar level to that of LTO-O. For Mo-LTO-R, even though part of the Ti^{4+} is reduced to Ti^{3+}, the extra charge was delocalised over the entire lattice due to the charge compensation by the high valence Mo dopant, thus resulting in enhanced stability.

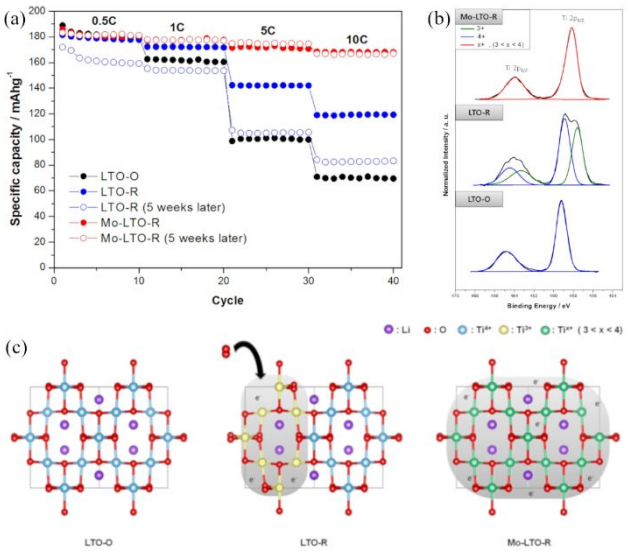

Figure 19. (a) Rate capability, (b) Ti 2p XPS spectra and (c) schematic images of pristine $Li_4Ti_5O_{12}$, Mo-doped OV-containing $Li_4Ti_5O_{12}$ and non-doped OV-containing $Li_4Ti_5O_{12}$. Reproduce with permission [86]. Copyright 2014, Springer Nature.

4.3.3 Interplay between OVs and amorphisation

In addition to crystalline electrode materials, amorphous electrode materials can benefit from OVs and their electrochemical performance can be boosted. Compared to the amorphous OV-free SnO_2 anneals in air [39], amorphous oxygen deficient SnO_2 (Fig. 20a) was obtained by annealing in N_2 and showed lower interface resistance, charge transfer resistance and charge transport resistance (Fig. 20b) for storing Na^+, and thus exhibited improved rate capability with delivering 330, 300, 277, 253, 225, 210 and 200 mAh g^{-1} at 0.2, 0.5, 1, 2, 5, 10 and 20 A g^{-1}, respectively (Fig. 20c). In comparison, OV-free counterpart practically failed when the current density increased to 5 A g^{-1} and higher. Ni et al. investigated the synergistic effect of amorphisation and OVs in SIBs [151]. The enhancement derived from amorphisation (a-Ar-Nb_2O_5, Fig. 20d) was not as obvious as that derived from OVs (c-H-Nb_2O_5) even though their cycle stability was similar. However, when amorphisation and OVs were combined (a-H-Nb_2O_5), the electrode delivered a capacity of 133 mAh g^{-1} after 1000 cycles at 2 C, being much higher than its counterparts. a-H-Nb_2O_5 also displayed higher capacities at both low rate (185 mAh g^{-1} at 0.5 C) and high rate (84 mAh

g^{-1} at 10 C) (Fig. 20e). It is worth noting that although c-H-Nb_2O_5 had a higher electronic conductivity (1.0×10^{-2} S cm^{-1}) than a-H-Nb_2O_5 (3.0×10^{-3} S cm^{-1}), the D_{Na} of the latter was much greater than that of the former (Fig. 20f). Therefore, a larger D_{Na} can outweigh a higher electronic conductivity, which was enabled by the co-existence of OVs and the amorphisation of Nb_2O_5. An OV-rich disordered TiO_2 layer was formed by a heat treatment in H_2 (H-TiO_2-C) to bridge the inner core of crystalline TiO_2 and the outer layer of carbon coating (Fig. 20g) [152], and the OV-rich disordered layer has a dual function in storing K^+. First, the adsorption energy of K^+ on the OV-rich disordered layer was calculated to be -1.718 eV (Fig. 20h), which is much higher than that of crystalline TiO_2 layer (-0.897 eV). Second, the K^+ migration energy barrier on the OV-rich disordered layer/carbon interface is calculated to be -2.035 eV, which is much lower than that of the crystalline TiO_2/carbon interface (-2.891 eV). This suggests the presence of the disordered layer could favour K^+ diffusion and enhance K^+ storage capability. As a result, H-TiO_2-C delivered a capacity of 197.5 mAh g^{-1} after 200 cycles with capacity retention of 82.1% at 100 mA g^{-1}, and it also retained capacities of 114.6 and 97.3 mAh g^{-1} at 1 and 2 A g^{-1}, respectively (Fig. 20i). Both the capacity and rate capability outperformed the control samples (TiO_2-C and TiO_2).

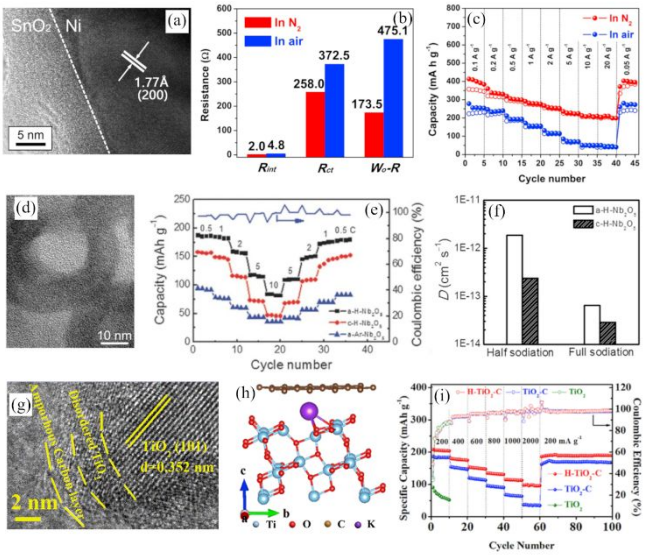

Figure 20. (a) HRTEM image of amorphous oxygen deficient SnO_2; (b) resistance and (c) rate capability of amorphous SnO_2 and amorphous oxygen deficient SnO_2. Reproduce with permission [39]. Copyright 2017, Elsevier. (d) HRTEM image of amorphous oxygen deficient Nb_2O_5; (e) rate capability of amorphous oxygen deficient Nb_2O_5, crystalline oxygen deficient Nb_2O_5 and amorphous Nb_2O_5; (f) diffusion coefficient of Na^+ in amorphous oxygen deficient Nb_2O_5 and crystaslline oxygen deficient Nb_2O_5. Reproduce with permission [151]. Copyright 2017, Wiley-VCH. (g) HRTEM image and (h) schematic image of OV-rich disordered; (i) rate capability of pristine TiO_2, carbon coated TiO_2 and TiO_2 with disordered layer. Reproduce with permission [152]. Copyright 2019, Elsevier.

4.3.4 Interplay between OVs and structural transformation

Electrode materials with a high crystallinity often suffer from the rigid crystal structure, a limited buffering capacity to accommodate ions, and sometimes structural pulverisation upon repetitive ion insertion/extraction. This is particularly critical for ion-batteries using large sized ions as charge carriers. We have discussed in the last section that amorphous materials with OVs can reduce charge transfer and transport resistance and increase Na^+/K^+ diffusion coefficient, and these benefits could outweigh the intrinsically low electronic conductivity of the materials. We highlight in this section that the synergistic effect between OVs and an amorphous structure could also have a profound role in altering the ion storage mechanism of electrode materials. Lao et al. synthesised an oxygen-deficient loose-layered potassium titanate (LL-KTO) $K(TiO_{1.875})_4OH$ (Fig. 21a) via inheriting the OVs from the precursor anatase TiO_{2-x} [153], and the authors demonstrated that the preservation of OVs relaxed the structure of LL-KTO to a great extent; as a result, LL-KTO showed a distinct ion storage mechanism involving a process of "stacked ↔ sliced structural transformation", which is neither an intercalation nor conversion or alloying process. As shown in Fig. 21b, during charging, the repulsion force gradually delaminated LL-KTO into oxygen-deficient lepidocrocite TiO_{2-x} nanosheets as K^+ leaves the structure ("sliced"). Some of the nanosheets self-aggregated through interlayer attractions and formed nuclei that appear as nanodots. In the subsequent discharging process, K+ is stored onto the nanosheets through liquid-diffusion while they stack back layer-by-layer into LL-KTO around the nuclei

("stacked"). Calculations showed that the interplay of OVs and K^+ is crucial to the stacked ↔ sliced structural transformation. As seen from the structural energies of lepidocrocite layered structures at various charging stages (Fig. 21c), the positive energy of $TiO_{1.875}$ (TiO_{2-x}) suggested that OVs made it metastable and hence susceptible to delamination that can be stabilised as nanosheets or nanodots. When increasing K^+ concentration, the structural energies became more negative, suggesting K^+ can stabilise the laminar structure. The synergistic role of OVs was further evidenced by the results that OV-free KTO cannot be delaminated upon complete removal of K^+ in the charged state (stoichiometric TiO_2). The proposed layer-by-layer storage dynamics can provide more accessible storage sites and net-zero structural deterioration, and therefore LL-KTO delivered the capacities of 201 and 183 mAh g^{-1} over 1800 cycles at 100 and 500 mA g^{-1}, respectively, outperforming other KTOs in PIBs and being comparable to titanium oxides in SIBs and LIBs.

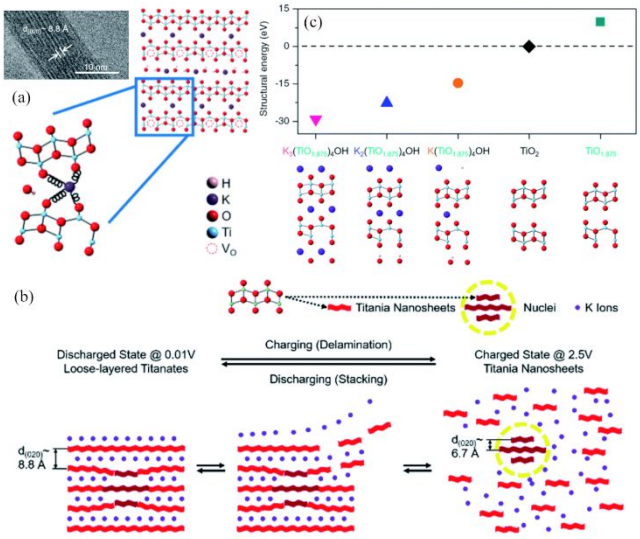

Figure 21. (a) TEM and schematic images of oxygen-deficient loose-layered potassium titanate; (b) schematic image of "stacked ↔ sliced structural transformation"; (c) structural energy of various stages between charge and discharge state and their corresponding schematic images. Reproduce with permission [153]. Copyright 2020, Royal Society of Chemistry.

4.3.5 Interplay between OVs and nanostructuring

A well-designed nanostructure enables a large surface area of metal oxides, which not only favours electrolyte penetration and shortens ion transport path but also amplifies the benefits of OVs [52,154]. Xu et al. investigated the electrochemical performance of oxygen deficient $BiVO_4$ nanostructures with various sizes (400, 50 and 5 nm) as SIB anodes [155]. The $BiVO_4$ nanocrystals with the size of 5 nm showed a black colour due to the presence of OVs (Fig. 22a), which is different from the yellow colour of the OV-free counterpart. Oxygen deficient $BiVO_4$ exhibited better cycle stability than pristine $BiVO_4$ with the same particle size, and more importantly the battery performance of oxygen deficient $BiVO_4$ was comprehensively enhanced with decreasing the particle size, with BVO@rGO-5 delivering the highest capacity and capacity retention as well as the best rate capability (Fig. 22b and 22c). This was attributed to the reduced R_{ct} (313, 128 and 87 Ω for 400, 50 and 5 nm, respectively), the increased D_{Na} (1.3×10^{-15}, 3.1×10^{-15} and 6.3×10^{-15} cm^2 s^{-1} for 400, 50 and 5 nm, respectively), and the improved surface-controlled kinetics (*b* value of 0.55,0.75 and 0.97 for 400, 50 and 5 nm, respectively) when downsizing the particles. WO_3 with both a mesoporous nanostructure and OVs (m-$W_{18}O_{49}$, pore size of ~4 nm as indicated by the white circles in Fig. 22d) outperformed the counterparts with either a mesoporous structure (m-WO_3) or OVs (b-$W_{18}O_{49}$) [154]. m-$W_{18}O_{49}$ delivered capacities of 1100.1 mAh g^{-1} at 0.1 A g^{-1} and 527.8 mAh g^{-1} at 1 A g^{-1} (Fig. 22e and 22f), while m-WO_3 and b-$W_{18}O_{49}$ showed severe capacity decay in the initial 20 cycles and retained < 200 mAh g^{-1} at high rates.

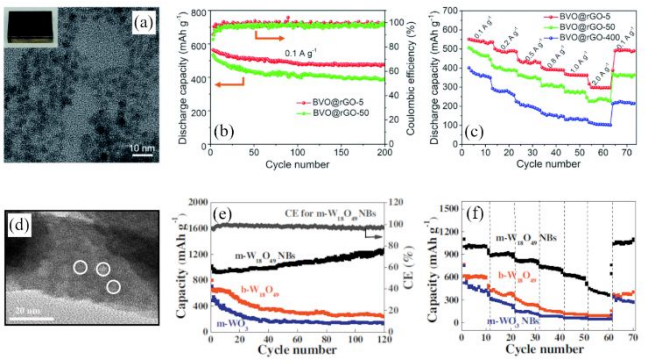

Figure 22. (a) TEM image of oxygen deficient $BiVO_4$ with the size of 5 nm; (b) cycling performance and (c) rate capability of oxygen deficient $BiVO_4$ samples. Reproduce with permission [155]. Copyright 2020, Royal Society of Chemistry.

(d) TEM image of mesoporous oxygen deficient WO_3; (e) cycling performance and (c) rate capability of $BiVO_4$ samples. Reproduce with permission [154]. Copyright 2016, Elsevier.

4.3.6 Interplay between OVs and functional coating

Despite the benefits of OVs towards enhanced battery performance, the stabilisation and/or protection of OVs should be taken into consideration when designing OVs in metal oxides. This is particularly critical for anode materials as they experience the formation of SEI layer that might negatively affect the functioning of OVs. A study has been discussed in section 4.4.1, where doping with foreign elements was used to achieve long-term stability of OVs in LTO. In this regard, another worth-mentioning study is to apply a thin surface protection layer onto oxygen deficient metal oxide electrodes. Xu et al. coated an ultrathin Al_2O_3 layer on oxygen deficient MoO_3 using atomic layer deposition (ALD) and applied the coated MoO_{3-x} as a SIB anode [156]. At a deep-discharge condition (0.01 V vs. Na^+/Na), the performance enhancement of MoO_3 was limited with the presence of OVs, as seen by the comparison between pristine MoO_3 (w-Mo) and MoO_{3-x} (b-Mo) samples (Fig. 23a and 23b). This was due to the SEI formation on the surface of the oxide electrodes. However, the performance enhancement was amplified after coating an ultrathin layer of Al_2O_3 (4 and 8 Å) on the electrode films, with the optimised coating thickness of 8 Å (b-Mo-8Al) delivering capacities of 230 mAh g^{-1} and 180 mAh g^{-1} at 0.5 A g^{-1} and 1 A g^{-1}, respectively. The XPS measurements demonstrated that peaks associated with the electrolyte decomposition products, e.g., alkyl, alkoxy, carbonated and ether, were suppressed with the Al_2O_3 coatings (Fig. 23c and 23d), suggesting a mechanically stable substitute for SEI and the inhibition of the formation of thick SEI. The authors attributed the observed enhancement to the presence of OVs that increased electronic conductivity and D_{Na} and more critically the Al_2O_3 coating that acted as an artificial SEI layer to effectively reduce the cycling-induced SEI layer and guarantee the proper functioning of OVs over the cycles.

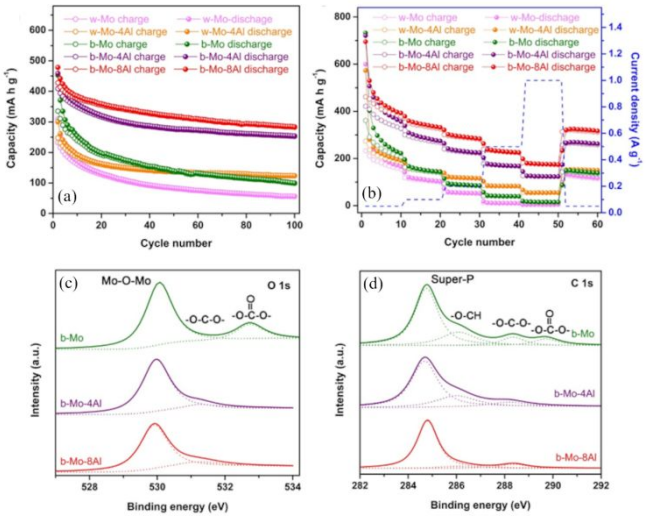

Figure 23. (a) Cycling performance and (b) rate capability of coated MoO_{3-x} samples; (c) C 1s and (d) O 1s XPS spectra of coated MoO_{3-x} samples after 100 cycles at 0.2 A g^{-1}. Reproduce with permission [156]. Copyright 2015, Wiley-VCH.

4.3.7 Interplay between OVs and transition metal deficiency

OVs can have synergistic effects with other types of vacancy. It has been reported that layered SIB cathodes experience phase change between O and P structures during (de)sodiation, which can cause irreversible capacity and performance fading. Unlike the study of $Na_{0.9}Ni_{0.3}Co_{0.15}Mn_{0.05}Ti_{0.5}O_2$ discussed in section 4.1.4, where OVs facilitated the reversible phase change between O3 and P3 structures, Xiao et al. introduced both oxygen and transition metal (TM) vacancies to $Na_x[(Mn_{0.66}Co_{0.17}Ni_{0.17})_{0.8}]O_{2-y}$, and the synergistic effect between the two types of vacancies not only stabilised the O3 structure of the cathode but also maintained it during cycling [157]. The authors used in situ XRD to trace the phase evolution during cycling (Fig. 24a). The O3 (003) peak moved between 1.38° and 1.25° due to the plane expansion (sodiation) and contraction (desodiation), which was outside the range of P3 (003) peak (1.15°-1.2°). Similar phenomenon was observed in the O3 (101), (012) and (113) peaks. The authors attributed the stabilisation of O3 to the lower migration barrier of TMs. The presence of TM and O

vacancies enabled easy migration of TM, which was verified by Fourier-transformed EXAFS. The O3-P3 phase change was normally triggered by TMO_2 layer gliding during de-sodiation. However, the migration of TMs impeded this global gliding. Once P3 site was formed locally, the interface between O3 and P3 tended to transform into a metastable distorted site, forcing the evolution of O3-P3 to experience a metastable pathway (Fig. 24b) and finally inhibiting the transformation from O3 to P3. Due to the stabilisation of O3, the SIB cathode achieved a high reversible capacity (160 mAh g^{-1}) and good cycling stability (86% capacity retention over 250 cycles).

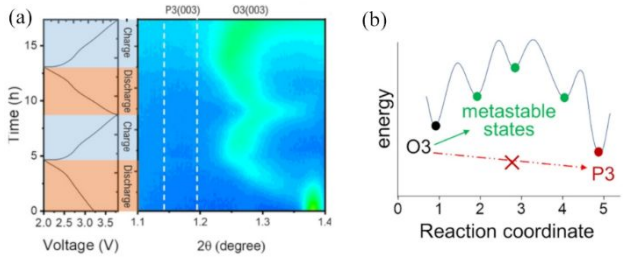

Figure 24. (a) In-situ XRD patterns of $Na_x[(Mn_{0.66}Co_{0.17}Ni_{0.17})_{0.8}]O_{2-y}$ electrode during initial two cycles at 12 mA g^{-1}; (b) energy path of the transformation from O3 to P3 structure in $Na_x[(Mn_{0.66}Co_{0.17}Ni_{0.17})_{0.8}]O_{2-y}$ sample. Reproduce with permission [157]. Copyright 2021, Wiley-VCH.

5 Summary and perspectives

In this review, we summarise the most widely used synthesis strategies and characterisation techniques of oxygen deficient metal oxides. More importantly, the roles of OVs in metal oxides are carefully summarised, which includes direct roles of OVs and synergistic roles of OVs with other contributors. The latter could open up new possibilities to enhance the electrochemical performance of metal oxides for rechargeable ion battery applications. Many oxygen deficient metal oxides have been reported as electrodes for rechargeable ion batteries so far and although remarkable progress has been made in understanding OVs' benefits to promote the use of metal oxide electrodes, there still exist obstacles to overcome and scientific questions to be addressed.

(1) The spatial effect of OVs

A great deal of knowledge about the OVs' role has been accumulated from the battery research so far, but there has been very little understanding on how the location/distribution of OVs in electrode materials affects the electrochemical performance of the electrode materials. What can be learnt from photocatalysis research is that the functioning of OVs is sensitive to where they are situated inside a metal oxide [101-102]. It could be expected that such kind of spatial effect certainly exists when investigating battery electrode materials. As a result, it is important to develop synthesis methods that can situate OVs at desirable locations inside metal oxides. OVs are often seen on the surface of oxides, so synthesis methods need to be designed in a way that OVs could be formed at the initial stage of nucleation and growth of oxides, which might enable OVs to be situated towards the bulk structure of oxides and in a better scenario, form a concentration gradient between the surface and bulk structure. Realising the control of OVs' location/distribution can allow us to differentiate the charge/discharge behaviour of the metal oxides, which is caused by the spatial effect of OVs and it in turn allows us to understand the precise corelation between the presence of OVs, their location/distribution, and electrochemical performance. To facilitate the study of the spatial effect, characterisation techniques should be orchestrated to deliver a complete and accurate picture of OVs, where results from various characterisations complement to each other and if possible, characterisations with an atomic resolution and imaging techniques should be encouraged to visualise OVs.

(2) The stability and evolution of OVs

As seen from literature, primary focus has been the generation of OVs by altering synthesis conditions and the subsequent battery performance of metal oxide electrodes. Characterisation of OVs verifies their presence only at the pristine state of the oxides, but the stability and evolution of

OVs during charge/discharge cycles have been receiving much less attention, which means little has been known how OVs change between the pristine and end states during an electrochemical process, and such information is critical to understand the electrochemical process during battery use. Given that the diffusion and condensation of OVs have been observed during the electrochemical cycle of intercalation-type electrodes [109], it is reasonable to expect more complexity of the evolution of OVs occurring in oxide electrodes that undergo a conversion or alloying reaction, where a major structural reconstruction takes place. Will OVs be presence after the reconstruction? How do OVs migration or change during the reconstruction? Will OVs stabilise the structure and lead to enhanced electrochemical performance? Or will OVs cause microcracks and lead to degraded performance? Many questions remain unanswered when considering battery charge/discharge is a dynamic process and OVs most likely evolve with the process. Although it is challenging to investigate the stability and evolution of OVs during an electrochemical cycle and it certainly requires advanced characterisation techniques, particularly in-situ techniques, to record the evolution, it is of great necessity to trace any possible change of OVs, which can be reflected back to initial material design and better guide material synthesis.

(3) The modelling and machine learning of OVs

The theoretical modelling of OVs in electrode materials involves models for the locating sites of OVs, the concentration of OVs, the solid diffusion of ions in OV-containing materials, the electronic conduction of the materials, the electrochemical reaction occurring in the materials, physical-chemical coupling during the reaction, and thermodynamic models of phase change if needed. Some of these have been elaborated in the main text, showcasing the powerful role of modelling. In line with the urgent need to investigate the stability and evolution of OVs during battery cycles, modelling is undoubtedly essential to provide accurate and efficient simulations of factors of interest, including but not limited to the crystallographic sites and distribution of OVs and the structural/phase change of electrode materials during a charge or discharge process, which might eventually cause the change of OVs. In return, simulations can accelerate the pace and efficiency of material synthesis and guide experimentation. Building on the knowledge accumulated through modelling-guide experimentation, machine learning could be a step-change approach to design OV-containing electrode materials. It is challenging due to the complexity of the electrochemical reactions taking place in the materials, which could be further complicated by how to make sense of big data collected from various type of materials and transfer the knowledge to the design of a specific material. However, machine learning will bring a step change in establishing the relationship of OVs – microstructure and type of materials – battery performance for forward prediction and inverse design.

(4) The use of OVs in multivalent-ion batteries

As highlighted throughout this review, the major development of OVs in metal oxide electrode materials are rooted in monovalent-ion batteries (LIBs, SIBs and PIBs), which highlights the roles of OVs in directly regulating the intrinsic properties of metal oxide electrodes, acting as a coating layer, and interplaying with various contributors. With these knowledges established, OVs have been demonstrated beneficial for metal oxides in divalent-ion batteries (ZIBs) [58,92], performing roles that are similar to what have been observed for monovalent-ion batteries. Because different types of batteries share similar fundamental charge transfer/transport processes, it is reasonable to expect that OVs could enhance the performance of other divalent-ion batteries (e.g., Ca^{2+} and Mg^{2+}) and even trivalent-ion batteries (e.g., Al^{3+}) in other similar ways discussed in this review, even though studies in this regard have been scarce. However, solid-state chemistry and electrochemistry of multivalent ions are substantially

more complex than that of monovalent alkali ions. Particularly, primary concern might shift from size effect (Li^+ vs. Na^+ vs. K^+) to charge density effect (charge over size). For instance, Ca^{2+} has a similar size as Na^+ but the charge is doubled, resulting in almost doubled charge density that can cause the structural deformation of metal oxides during ion diffusion or even electrochemical inactivity. Therefore, OVs may not work in a similar way for multivalent-ion batteries as for monovalent-ion batteries. It is obvious that phase change of metal oxide electrodes can be quite different between ions with different charge densities. OVs could interplay differently with amorphisation and structural transformation when charge carrier changes from monovalent to multivalent, due to the different structural deformation caused by the two types of ions. In this regard, it is of great urgence and importance to start investigating the roles of OVs in multivalent-ion batteries. It will not only overcome a major obstacle of solid-state diffusion but also further our understanding of the interaction between a defective structure and high charge-density ions, which would not be achieved in monovalent-ion batteries.

Oxygen vacancy is one of the most common but powerful defects in battery electrode materials. The substantial progress achieved to date from OV-containing electrodes has undoubtedly solidified the promise that OVs hold. Thus, it is of great importance to continue investigating OVs in-depth. The knowledge obtained from the investigation could be transferred to the study of other types of point defects (e.g., anionic and cationic vacancies) and even line and plane defects, which could potentially deliver knowledge that is initially unknown. We hope this review could provide a useful platform to study OVs for the battery community and in a wider sense, provide insights into the utilisation of OVs for other research communities.

Acknowledgements Y.X. acknowledges the support from the Engineering and Physical Sciences Research Council (grant no. EP/V000152/1).

Author contributions Conceptualisation, R.Z.W. and Y.X.; Writing – Original Draft, R.Z.W.; Writing – Review & Editing, R.Z.W., Y.L., and Y.X.; Supervision and Funding Acquisition, Y.X.

Declaration of interests The authors declare no competing interests.

Reference

1. Cheng F, Liang J, Tao Z, Chen J. *Adv Mater*, 2011, 23: 1695–1715
2. Dunn B, Kamath H, Tarascon JM. *Science (80-)*, 2011, 334: 928–935
3. Larcher D, Tarascon JM. *Nat Chem*, 2015, 7: 19–29
4. Wang L, Xie X, Dinh KN, Yan Q, Ma J. *Coord Chem Rev*, 2019, 397: 138–167
5. Kim SW, Seo DH, Ma X, Ceder G, Kang K. *Adv Energy Mater*, 2012, 2: 710–721
6. Hosaka T, Kubota K, Hameed AS, Komaba S. *Chem Rev*, 2014, 114: 11636–11682
7. Nayak PK, Yang L, Brehm W, Adelhelm P. *Angew Chemie - Int Ed*, 2018, 57: 102–120
8. Hwang JY, Myung ST, Sun YK. *Chem Soc Rev*, 2017, 46: 3529–3614
9. Hosaka T, Kubota K, Hameed AS, Komaba S. *Chem Rev*, 2020, 120: 6358–6466
10. Zhang W, Liu Y, Guo Z. *Sci Adv*, 2019, 5: eaav7412
11. Rajagopalan R, Tang Y, Ji X, Jia C, Wang H. *Adv Funct Mater*, 2020, 30: 1909486
12. Zhang N, Chen X, Yu M, Niu Z, Cheng F, Chen J. *Chem Soc Rev*, 2020, 49: 4203–4219
13. Tang B, Shan L, Liang S, Zhou J. *Energy Environ Sci*, 2019, 12: 3288–3304
14. Jia X, Liu C, Neale ZG, Yang J, Cao G. *Chem Rev*, 2020, 120: 7795–7866
15. Vaalma C, Buchholz D, Weil M, Passerini S. *Nat Rev Mater*, 2018, 3: 18013
16. Yan Z, Obrovac MN. *J Power Sources*, 2020, 464: 228228
17. Eftekhari A. *ACS Sustain Chem Eng*, 2019, 7: 3684–3687
18. Zhang X, Liu X, Zeng Y, Tong Y, Lu X. *Small Methods*, 2020: 1900823
19. Wang D, Choi D, Li J, Yang Z, Nie Z, Kou R, Hu D, Wang C, Saraf L V., Zhang J, Aksay IA, Liu J. *ACS Nano*, 2009, 3: 907–914
20. Xia Y, Xiao Z, Dou X, Huang H, Lu X, Yan R, Gan Y, Zhu W, Tu J, Zhang W, Tao X. *ACS Nano*, 2013, 7: 7083–7092
21. Wang L, Wei Z, Mao M, Wang H, Li Y, Ma J. *Energy Storage Mater*, 2019, 16: 434–454
22. Wu ZS, Zhou G, Yin LC, Ren W, Li F, Cheng HM. *Nano Energy*, 2012, 1: 107–131
23. Ji L, Meduri P, Agubra V, Xiao X, Alcoutlabi M. *Adv Energy Mater*,

2016, 6: 1502159
24. Wu H Bin, Chen JS, Hng HH, Lou XW. *Nanoscale*, 2012, 4: 2526–2542
25. Zheng J, Xiao J, Zhang JG. *Nano Today*, 2016, 11: 678–694
26. Greiner MT, Chai L, Helander MG, Tang WM, Lu ZH. *Adv Funct Mater*, 2012, 22: 4557–4568
27. Liu Y, Xiao C, Li Z, Xie Y. *Adv Energy Mater*, 2016, 6: 1600436
28. Wang Y, Xiao X, Li Q, Pang H. *Small*, 2018, 14: 1802193
29. Zhang Y, Ding Z, Foster CW, Banks CE, Qiu X, Ji X. *Adv Funct Mater*, 2017, 27: 1700856
30. Ma D, Li Y, Zhang P, Lin Z. *ChemSusChem*, 2018, 11: 3693–3703
31. Kim HS, Cook JB, Lin H, Ko JS, Tolbert SH, Ozolins V, Dunn B. *Nat Mater*, 2017, 16: 454–462
32. Nagoshi M, Suzuki T, Fukuda Y, Terashima K, Nakanishi Y, Ogita M, Tokiwa A, Syono Y, Tachiki M. *Phys Rev B*, 1991, 43: 10445–10450
33. Barsan N, Weimar U. *J Electroceramics*, 2001, 7: 143–167
34. Degler D, Wicker S, Weimar U, Barsan N. *J Phys Chem C*, 2015, 119: 11792–11799
35. Wu Y, Jiang Y, Shi J, Gu L, Yu Y. *Small*, 2017, 13: 1700129
36. Bin D, Wen Y, Yuan Y, Liu Y, Wang Y, Wang C, Xia Y. *Electrochim Acta*, 2019, 320: 134555
37. Pan X, Yang MQ, Fu X, Zhang N, Xu YJ. *Nanoscale*, 2013, 5: 3601–3614
38. Wang J, Chen R, Xiang L, Komarneni S. *Ceram Int*, 2018, 44: 7357–7377
39. Xu Y, Zhou M, Zhang C, Wang C, Liang L, Fang Y, Wu M, Cheng L, Lei Y. *Nano Energy*, 2017, 38: 304–312
40. Liu Y, Zhang H, Wan H, Zhang W, Jiang N, Huang G, Wang Z, Luo S, Sun H. *J Alloys Compd*, 2019, 787: 720–727
41. Luo JY, Chen LJ, Zhao YJ, He P, Xia YY. *J Power Sources*, 2009, 194: 1075–1080
42. Xu Z, Wang J, Zhang K, Zheng H, Dai ZX, Gui J, Yang XQ. *ACS Appl Mater Interfaces*, 2014, 6: 1219–1227
43. Shin JY, Joo JH, Samuelis D, Maier J. *Chem Mater*, 2012, 24: 543–551
44. Lu X, Mao Q, Chen Y, Bao L, Tong L, Xiong Q, Qin H, Pan H, Ji Z. *Electrochim Acta*, 2018, 282: 351–361
45. Zou Y, Zhang W, Chen N, Chen S, Xu W, Cai R, Brown CL, Yang D, Yao X. *ACS Nano*, 2019, 13: 2062–2071
46. Abouimrane A, Compton OC, Deng H, Belharouak I, Dikin DA, Nguyen ST, Amine K. *Electrochem Solid-State Lett*, 2011, 14: A126-A129
47. Cronemeyer DC. *Phys Rev*, 1959, 113: 1222–1226
48. Ventosa E, Tymoczko A, Xie K, Xia W, Muhler M, Schuhmann W. *ChemSusChem*, 2014, 7: 2584–2589
49. Ma L, Gao X, Zhang W, Yuan H, Hu Y, Zhu G, Chen R, Chen T, Tie Z, Liu J, Wu T, Jin Z. *Nano Energy*, 2018, 53: 91–96
50. Tan X, Liu R, Xie C, Shen Q. *J Power Sources*, 2018, 374: 134–141
51. Zeng Y, Lai Z, Han Y, Zhang H, Xie S, Lu X. *Adv Mater*, 2018, 30: 1802396
52. Teng C, Yang F, Sun M, Yin K, Huang Q, Fu G, Zhang C, Lu X, Jiang J. *Chem Sci*, 2019, 10: 7600–7609
53. Li Y, Wang D, An Q, Ren B, Rong Y, Yao Y. *J Mater Chem A*, 2016, 4: 5402–5405
54. Shi Y, Zhang D, Chang C, Huang K, Holze R. *J Alloys Compd*, 2015, 639: 274–279
55. Kubota K, Kaneko T, Hirayama M, Yonemura M, Imanari Y, Nakane K, Kanno R. *J Power Sources*, 2012, 216: 249–255
56. He H, Zhang Q, Wang H, Zhang H, Li J, Peng Z, Tang Y, Shao M. *J Power Sources*, 2017, 354: 179–188
57. Yang C, Liu X, Yang Z, Gu L, Yu Y. *Adv Mater Interfaces*, 2016, 3: 1600730
58. Lu Y, Wang J, Zeng S, Zhou L, Xu W, Zheng D, Liu J, Zeng Y, Lu X. *J Mater Chem A*, 2019, 7: 21678–21683
59. Chen B, Zhao B, Zhou J, Fang Z, Huang Y, Zhu X, Sun Y. *J Mater Sci Technol*, 2019, 35: 994–1002
60. Xiong T, Yu ZG, Wu H, Du Y, Xie Q, Chen J, Zhang YW, Pennycook SJ, Lee WSV, Xue J. *Adv Energy Mater*, 2019, 9: 1803815
61. Sun Z, Yang C, Liu G, Lu H, Zhang R, Wang L, Wang H. *Electrochim Acta*, 2017, 239: 16–24
62. Wang Y, Xue X, Liu P, Wang C, Yi X, Hu Y, Ma L, Zhu G, Chen R, Chen T, Ma J, Liu J, Jin Z. *ACS Nano*, 2018, 12: 12492–12502
63. Zheng J, Yang R, Xie L, Jianglan Q, Yang L, Xingguo L. *Adv Mater*, 2010, 22: 1451–1473
64. Dou S, Tao L, Wang R, El Hankari S, Chen R, Wang S. *Adv Mater*, 2018, 30: 1705850
65. Xu L, Jiang Q, Xiao Z, Li X, Huo J, Wang S, Dai L. *Angew Chemie - Int Ed*, 2016, 55: 5277–5281
66. Liang K, He H, Ren Y, Luan J, Wang H, Ren Y, Huang X. 2020, 1739–1747
67. Zhang G, Xiong T, Yan M, He L, Liao X, He C, Yin C, Zhang H, Mai L. *Nano Energy*, 2018, 49: 555–563
68. Lan CK, Chuang SI, Bao Q, Liao YT, Duh JG. *J Power Sources*, 2015, 275: 660–667
69. Zhu C, Li C, Zheng M, Delaunay JJ. *ACS Appl Mater Interfaces*, 2015, 7: 22355–22363
70. Zhang T, Cui S, Yu B, Liu Z, Wang D. *Chem Commun*, 2015, 51: 16940–16943
71. Zhang C, Song H, Liu C, Liu Y, Zhang C, Nan X, Cao G. *Adv Funct Mater*, 2015, 25: 3497–3504
72. Yang W, Dong L, Yang W, Xu C, Shao G, Wang G. *Small Methods*, 2020, 4: 1900670
73. Li Z, Dong Y, Feng J, Xu T, Ren H, Gao C, Li Y, Cheng M, Wu W, Wu M. *ACS Nano*, 2019, 13: 9227–9236
74. Guan D, Yu Q, Xu C, Tang C, Zhou L, Zhao D, Mai L. *Nano Res*, 2017, 10: 4351–4359
75. Zhang Q, Wei Y, Yang H, Su D, Ma Y, Li H, Zhai T. *ACS Appl Mater Interfaces*, 2017, 9: 7009–7016
76. Wu N, Qiao X, Shen J, Liu G, Sun T, Wu H, Hou H, Liu X, Zhang Y,

Ji X. *Electrochim Acta*, 2019, 299: 540–548
77. Sun Y, Zan L, Zhang Y. *Appl Surf Sci*, 2019, 483: 270–277
78. Ni Q, Dong R, Bai Y, Wang Z, Ren H, Sean S, Wu F, Xu H, Wu C. *Energy Storage Mater*, 2020, 25: 903–911
79. Zhao Q, Bi R, Cui J, Yang X, Zhang L. *ACS Appl Energy Mater*, 2018, 1: 4459–4466
80. Xia J, Zhao H, Pang WK, Yin Z, Zhou B, He G, Guo Z, Du Y. *Chem Sci*, 2018, 9: 3421–3425
81. Li Q, Feng Y, Wang P, Che R. *Nanoscale*, 2019, 11: 5080–5093
82. Li Q, Zhao Y, Liu H, Xu P, Yang L, Pei K, Zeng Q, Feng Y, Wang P, Che R. *ACS Nano*, 2019, 13: 11921–11934
83. He H, Wang H, Sun D, Shao M, Huang X, Tang Y. *Electrochim Acta*, 2017, 236: 43–52
84. Chen Y, Cao X, Lin B, Gao B. *Appl Surf Sci*, 2013, 264: 845–852
85. Liu F, Cheng X, Xu R, Wu Y, Jiang Y, Yu Y. *Adv Funct Mater*, 2018, 28: 1800394
86. Song H, Jeong TG, Moon YH, Chun HH, Chung KY, Kim HS, Cho BW, Kim YT. *Sci Rep*, 2014, 4: 4350
87. Guan C, Liu X, Ren W, Li X, Cheng C, Wang J. *Adv Energy Mater*, 2017, 7: 1602391
88. Dupin JC, Gonbeau D, Vinatier P, Levasseur A. *Phys Chem Chem Phys*, 2000, 2: 1319–1324
89. Jain S, Shah J, Negi NS, Sharma C, Kotnala RK. *Int J Energy Res*, 2019, 43: 4743–4755
90. Kim JH, Jang YJ, Kim JH, Jang JW, Choi SH, Lee JS. *Nanoscale*, 2015, 7: 19144–19151
91. Yang J, Yang Z, Meng T, Han Y, Wang X, Zhang Q. *Phys Status Solidi Appl Mater Sci*, 2016, 213: 1010–1015
92. Fang G, Zhu C, Chen M, Zhou J, Tang B, Cao X, Zheng X, Pan A, Liang S. *Adv Funct Mater*, 2019, 29: 1808375
93. Kuzmin A, Chaboy J. *IUCrJ*, 2014, 1: 571–589
94. Zhou YN, Ma J, Hu E, Yu X, Gu L, Nam KW, Chen L, Wang Z, Yang XQ. *Nat Commun*, 2014, 5: 5381
95. Leedahl B, de Boer T, Yuan X, Moewes A. *Chem - A Eur J*, 2019, 25: 3272–3278
96. Jin L, Zheng X, Liu W, Cao L, Cao Y, Yao T, Wei S. *J Mater Chem A*, 2017, 5: 12022–12026
97. James Speight. Environmental Inorganic Chemistry for Engineers. 1st ed. Butterworth-Heinemann, 2017
98. Shu GJ, Tian JC, Lin CK, Hayashi M, Liou SC, Chen WT, Wong DP, Liou HL, Chou FC. *New J. Phys*, 2017, 19: 023026
99. Ye K, Li K, Lu Y, Guo Z, Ni N, Liu H, Huang Y, Ji H, Wang P. *TrAC - Trends Anal Chem*, 2019, 116: 102–108
100. Zheng J, Liu Y, Ji G, Zhang P, Cao X, Wang B, Zhang C, Zhou X, Zhu Y, Shi D. *ACS Appl Mater Interfaces*, 2015, 7: 23431–23438
101. Hou L, Zhang M, Guan Z, Li Q, Yang J. *Appl Surf Sci*, 2018, 428: 640–647
102. Li J, Zhang M, Guan Z, Li Q, He C, Yang J. *Appl Catal B Environ*, 2017, 206: 300–307
103. Yang S, Halliburton LE, Manivannan A, Bunton PH, Baker DB, Klemm M, Horn S, Fujishima A. *Appl Phys Lett*, 2009, 94: 2–5
104. Jiang X, Zhang Y, Jiang J, Rong Y, Wang Y, Wu Y, Pan C. *J Phys Chem C*, 2012, 116: 22619–22624
105. Kong M, Li Y, Chen X, Tian T, Fang P, Zheng F, Zhao X. *J Am Chem Soc*, 2011, 133: 16414–16417
106. Zhu Q, Wang X, Jiang J, Xu AW. *J Phys Chem C*, 2017, 121: 22806–22814
107. Dutta S, Chattopadhyay S, Jana D, Banerjee A, Manik S, Pradhan SK, Sutradhar M, Sarkar A. *J Appl Phys*, 2006, 100: 114328
108. Gao P, Wang Z, Fu W, Liao Z, Liu K, Wang W, Bai X, Wang E. *Micron*, 2010, 41: 301–305
109. Huang R, Ikuhara, Yumi H, Mizoguchi T, Findlay SD, Kuwabara A, Fisher CAJ, Moriwake H, Oki H, Hirayama T, Ikuhara Y. *Angew Chemie - Int Ed*, 2011, 50: 3053–3057
110. Yao L, Inkinen S, Van Dijken S. *Nat Commun*, 2017, 8: 14544
111. Baster D, Dybko K, Szot M, Świerczek K, Molenda J. *Solid State Ionics*, 2014, 262: 206–210
112. Chen J, Ding Z, Wang C, Hou H, Zhang Y, Wang C, Zou G, Ji X. *ACS Appl Mater Interfaces*, 2016, 8: 9142–9151
113. Yang Z, Sun J, Xie Y, Kaur P, Hernandez J, Ni Y, Yu Y, Varghese OK, Huang Y, Chen S. *J Mater Chem A*, 2018, 6: 22037–22042
114. Zhang J, Jiang H, Zeng Y, Zhang Y, Guo H. *J Power Sources*, 2019, 439: 227026
115. Zhang S, Liu G, Qiao W, Wang J, Ling L. *J Colloid Interface Sci*, 2020, 562: 193–203
116. Jiang L, Wu Z, Wang Y, Tian W, Yi Z, Cai C, Jiang Y, Hu L. *ACS Nano*, 2019, 13: 10376–10385
117. Zhang N, Cheng F, Liu Y, Zhao Q, Lei K, Chen C. *J Am Chem Soc*, 2016, 138: 12894–12901
118. Zhu C, Fang G, Zhou J, Guo J, Wang Z, Wang C, Li J, Tang Y, Liang S. *J Mater Chem A*, 2018, 6: 9677–9683
119. Song H, Luo M, Wang A. *ACS Appl Mater Interfaces*, 2017, 9: 2875–2882
120. Zhu J, Chen J, Xu H, Sun S, Xu Y, Zhou M, Gao X, Sun Z. *ACS Appl Mater Interfaces*, 2019, 11: 17384–17392
121. Hou C, Hou Y, Fan Y, Zhai Y, Wang Y, Sun Z, Fan R, Dang F, Wang J. *J Mater Chem A*, 2018, 6: 6967–6976
122. Chen J, Luo B, Chen Q, Li F, Guo Y, Wu T, Peng P, Qin X, Wu G, Cui M, Liu L, Chu L, Jiang B, Li Y, Gong X, Chai Y, Yang Y, Chen Y, Huang W, Liu X, Li M. *Adv Mater*, 2020, 1905578
123. Wang K, Zhang C, Fu H, Liu C, Li Z, Ma W, Lu X, Cao G. *Chem - A Eur J*, 2017, 23: 5368–5374
124. Yu DYW, Yanagida K, Kato Y, Nakamura H. *J Electrochem Soc*, 2009, 156: A417
125. Lim JM, Kim D, Lim YG, Park MS, Kim YJ, Cho M, Cho K. *ChemElectroChem*, 2016, 3: 943–949
126. Sun Y, Cong H, Zan L, Zhang Y. *ACS Appl Mater Interfaces*, 2017, 9: 38545–38555
127. Yoshio M, Xia Y, Sakai T. *Electrochemistry*, 2001, 69: 516–518
128. Cai Y, Ku L, Wang L, Ma Y, Zheng H, Xu W, Han J, Qu B, Chen Y,

Xie Q, Peng DL. *Sci China Mater*, 2019, 62: 1374–1384

129. Santhanam R, Rambabu B. *J Power Sources*, 2010, 195: 5442–5451
130. Sushko P V., Rosso KM, Zhang JG, Liu J, Sushko ML. *Adv Funct Mater*, 2013, 23: 5530–5535
131. Xiao J, Chen X, Sushko P V., Sushko ML, Kovarik L, Feng J, Deng Z, Zheng J, Graff GL, Nie Z, Choi D, Liu J, Zhang JG, Whittingham MS. *Adv Mater*, 2012, 24: 2109–2116
132. Liu H, Zhang X, He X, Senyshyn A, Wilken A, Zhou D, Fromm O, Niehoff P, Yan B, Li J, Muehlbauer M, Wang J, Schumacher G, Paillard E, Winter M, Li J. *J Electrochem Soc*, 2018, 165: A1886–A1896
133. Jiang K, Guo S, Pang WK, Zhang X, Fang T, Wang S fei, Wang F, Zhang X, He P, Zhou H. *Nano Res*, 2021, https://doi.org/10.1007/s12274-021-3349-4
134. Chen C, Geng T, Du C, Zuo P, Cheng X, Ma Y, Yin G. *J Power Sources*, 2016, 331: 91–99
135. Yang Z, Zhong J, Li J, Liu Y, Niu B, Kang F. *Ceram Int*, 2019, 45: 439–448
136. Yang K, Liu Y, Niu B, Yang Z, Li J. *Ionics (Kiel)*, 2018, 25: 2027–2034
137. Du P, Li T, Jiang X, Wang D, Zheng X. *J Alloys Compd*, 2020, 814: 152270
138. Zhao C, Cai Y, Yin K, Li H, Shen D, Qin N, Lu Z, Liu C, Wang HE. *Chem Eng J*, 2018, 350: 201–208
139. Ren Q, Qin N, Liu B, Yao Y, Zhao X, Deng Z, Li Y, Dong Y, Qian D, Su B-L, Zhang W, Wang H-E. *J Mater Chem A*, 2020, 8: 3450–3458
140. Bai YL, Xarapatgvl R, Wu XY, Liu X, Liu YS, Wang KX, Chen JS. *Nanoscale*, 2019, 11: 17860–17868
141. Gan Q, He H, Zhao K, He Z, Liu S, Yang S. *ACS Appl Mater Interfaces*, 2018, 10: 7031–7042
142. Gu M, Kushima A, Shao Y, Zhang JG, Liu J, Browning ND, Li J, Wang C. *Nano Lett*, 2013, 13: 5203–5211
143. Ma D, Li Y, Mi H, Luo S, Zhang P, Lin Z, Li J, Zhang H. *Angew Chemie - Int Ed*, 2018, 57: 8901–8905
144. Zhang H, Jiang Y, Qi Z, Zhong X, Yu Y. *Energy Storage Mater*, 2018, 12: 37–43
145. Wang D, Li X, Wang J, Yang J, Geng D, Li R, Cai M, Sham TK, Sun X. *J Phys Chem C*, 2012, 116: 22149–22156
146. Meng T, Li B, Hu L, Yang H, Fan W, Zhang S, Liu P, Li M, Gu FL, Tong Y. *Small Methods*, 2019, 3: 1900185
147. Wu N, Du W, Gao X, Zhao L, Liu G, Liu X, Wu H, He YB. *Nanoscale*, 2018, 10: 11460–11466
148. Ventosa E, Xia W, Klink S, Mantia F La, Mei B, Muhler M, Schuhmann W. *Chem - A Eur J*, 2013, 19: 14194–14199
149. Wang Q, He H, Luan J, Tang Y, Huang D, Peng Z, Wang H. *Electrochim Acta*, 2019, 309: 242–252
150. Wu Y, Wei Z, Xu R, Gong Y, Gu L, Ma J, Yu Y. *Nano Res*, 2019, 12: 2211–2217
151. Ni J, Wang W, Wu C, Liang H, Maier J, Yu Y, Li L. *Adv Mater*, 2017, 29: 1605607
152. Li Y, Yang C, Zheng F, Pan Q, Liu Y, Wang G, Liu T, Hu J, Liu M. *Nano Energy*, 2019, 59: 582–590
153. Lao CY, Yu Q, Hu J, Li N, Divitini G, Kim HK, Wang W (Alex), Liu Y, Chen X, Kumar RV. *J Mater Chem A*, 2020, 8: 17550–17557
154. Sun Y, Wang W, Qin J, Zhao D, Mao B, Xiao Y, Cao M. *Electrochim Acta*, 2016, 187: 329–339
155. Xu X, Xu Y, Xu F, Jiang G, Jian J, Yu H, Zhang E, Shchukin D, Kaskel S, Wang H. *J Mater Chem A*, 2020, 8: 1636–1645
156. Xu Y, Zhou M, Wang X, Wang C, Liang L, Grote F, Wu M, Mi Y, Lei Y. *Angew Chemie - Int Ed*, 2015, 54: 8768–8771
157. Xiao B, Wang Y, Tan S, Song M, Li X, Zhang Y, Lin F, Han KS, Omenya F, Amine K, Yang XQ, Reed D, Hu Y, Xu GL, Hu E, Li X, Li X. *Angew Chemie - Int Ed*, 2021, 60: 8258–8267

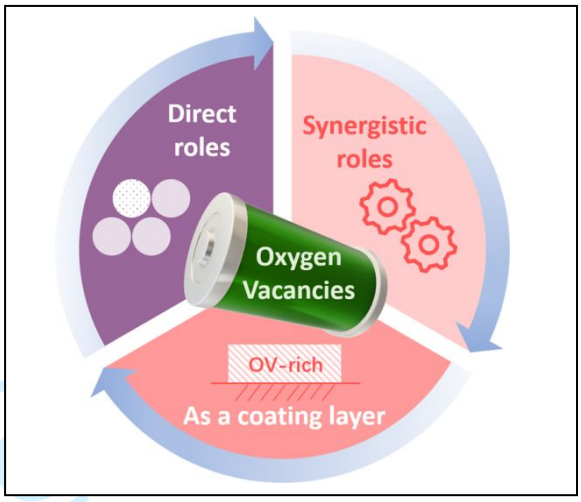

Table of Contents graphic